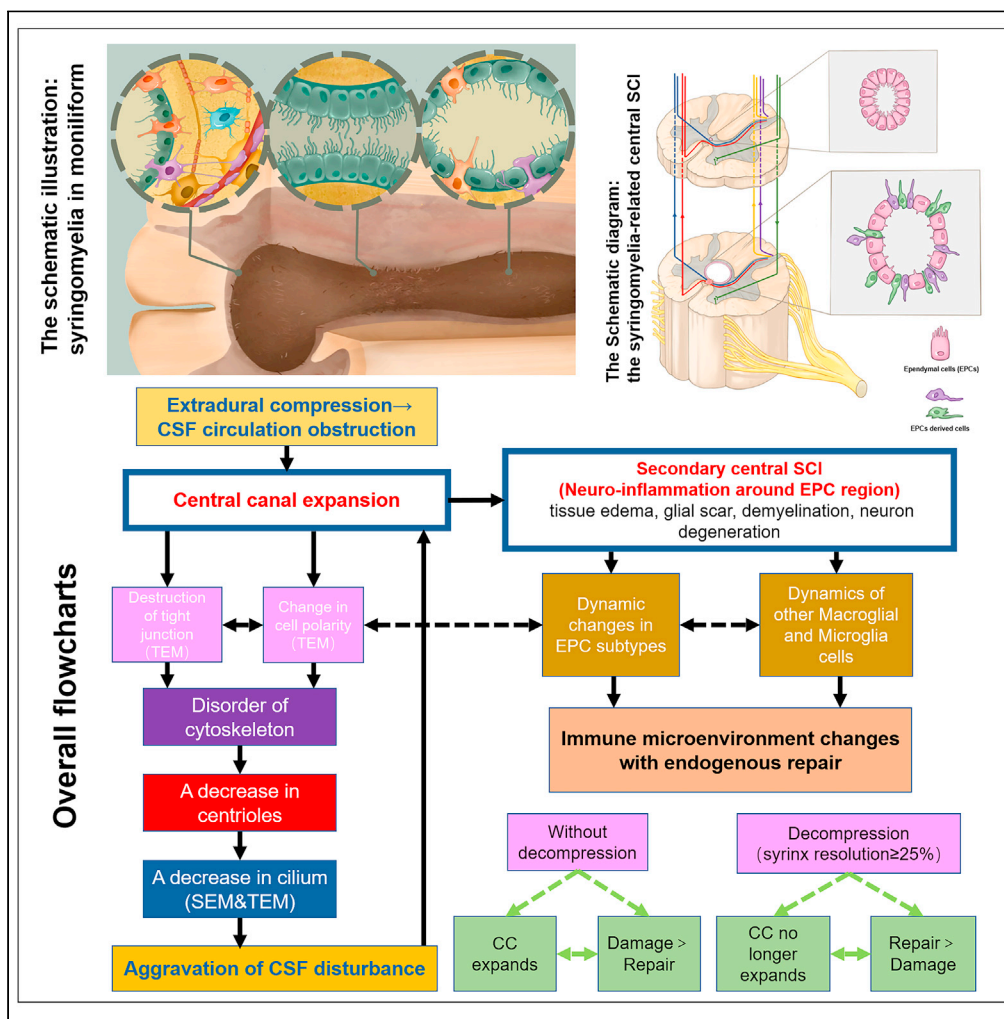


Article

Single-cell transcriptomics reveals ependymal subtypes related to cytoskeleton dynamics as the core driver of syringomyelia pathological development



Chunli Lu,
Xianming Wu,
Xinyu Wang,
Zhifeng Xiao,
Longbing Ma,
Jianwu Dai,
Fengzeng Jian

xianmingwu@genetics.ac.cn (X.W.)
jwdai@genetics.ac.cn (J.D.)
jianfengzeng@xwh.ccmu.edu.cn (F.J.)

Highlights

Dynamic pathophysiological changes during syringomyelia formation and resolution

Multiple cellular subtype alterations appear during syringomyelia development

Early effective decompression could benefit syrinx resolution and SCI recovery

Remodeling ependymal cytoskeleton as the focus for future treatment for syringomyelia



Article

Single-cell transcriptomics reveals ependymal subtypes related to cytoskeleton dynamics as the core driver of syringomyelia pathological development

Chunli Lu,^{1,2,3,4,5} Xianming Wu,^{6,*} Xinyu Wang,^{1,2,3,4,5} Zhifeng Xiao,⁶ Longbing Ma,^{1,2,3,4,5} Jianwu Dai,^{6,*} and Fengzeng Jian^{1,2,3,4,5,7,*}

SUMMARY

Syringomyelia is a common clinical lesion associated with cerebrospinal fluid flow abnormalities. By a reversible model with chronic extradural compression to mimic human canalicular syringomyelia, we explored the spatiotemporal pathological alterations during syrinx development. The most dynamic alterations were observed in ependymal cells (EPCs), oligodendrocyte lineage, and microglia, as a response to neuroinflammation. Among different cell types, EPC subtypes experienced obvious dynamic alterations, which were accompanied by ultrastructural changes involving the ependymal cytoskeleton, cilia, and dynamic injury in parenchyma primarily around the central canal, corresponding to the single-cell transcripts. After effective decompression, the syrinx resolved with the recovery of pathological damage and overall neurological function, implying that for syringomyelia in the early stage, there was still endogenous repair potential coexisting with immune microenvironment imbalance. Ependymal remodeling and cilia restoration might be important for better resolution of syringomyelia and parenchymal injury recovery.

INTRODUCTION

Syringomyelia is a common clinical lesion associated with arachnoid adhesion, traumatic injury, intramedullary tumor, and congenital or acquired spinal deformities.^{1,2} To distinguish it from a non-canalicular cyst at the primary injury region in acute traumatic events,³ the syringomyelia in the manifestation of the chronic dilation of the central canal (CC) is therefore known as canalicular syringomyelia, similar to chronic hydromyelia accompanied by secondary pathological changes of the spinal cord.⁴ Patients with syringomyelia in clinical practice will appear with a diverse range of symptoms and prognoses and have characteristics in common with central spinal cord syndrome.⁵ The mechanism of syringomyelia formation and resolution remains controversial. But according to earlier views,^{6,7} it was caused by a disruption in the cerebrospinal fluid (CSF) circulation. Canalicular syringomyelia, which is comparable to non-communicating hydrocephalus, has been demonstrated with considerable subarachnoid fibrosis and consequent CSF flow abnormalities recently.^{8,9} Previous research has shown that dysfunctional ependymal cilia may impair normal CSF flow, increasing the risk of hydrocephalus.¹⁰ However, there has never been any data on the involvement of abnormal ependymal cilia in syringomyelia development. In addition, the ependymal region around the CC is the niche for endogenous stem cells,^{11,12} indicating that utilizing its capacity of regeneration may be the subject of future study for syringomyelia recovery.³

The pathophysiological process underlying the onset, progression, and outcome of syringomyelia was still not entirely understood. That is why therapeutic efficacy for syringomyelia has not been significantly improved despite numerous relevant studies over the past few decades.^{13,14} We previously constructed a reversible model with chronic extradural compression by a microsurgical operation to reproduce canalicular syringomyelia in the human condition.¹⁵ The modeling syrinx came close to the usual moniliform-like morphology frequently observed in the clinic through preliminary pathological investigation.¹⁶ Moreover, it is intriguing to see that in our prior clinical study on a series of patients with syringomyelia, the symptom duration of moniliform syringomyelia is shorter than that of the dilated type.¹⁷ Most

¹Division of Spine, Department of Neurosurgery, Xuanwu Hospital, Capital Medical University (CCMU), Beijing, China

²Neurospine Center, China International Neuroscience Institute (CHINA-INI), Beijing, China

³Research Center of Spine and Spinal Cord, Beijing Institute of Brain Disorders, CCMU, Beijing, China

⁴Lab of Spinal Cord Injury and Function Reconstruction, CHINA-INI, Beijing, China

⁵National Center for Neurological Disorders, Beijing, China

⁶State Key Laboratory of Molecular Developmental Biology, Institute of Genetics and Developmental Biology, Chinese Academy of Sciences, Beijing 100101, China

⁷Lead contact

*Correspondence: xianmingwu@genetics.ac.cn (X.W.), jwdai@genetics.ac.cn (J.D.), jianfengzeng@xwh.ccmu.edu.cn (F.J.)

<https://doi.org/10.1016/j.isci.2023.106850>



moniliform syrinx resolved quickly the following decompression, compared to dilated syringomyelia, and these patients with better prognosis. We hypothesized that the special syrinx phenotype in moniliform configuration might represent an early reversible state.

Regarding the neuroinflammation damage including edema, glial scar, demyelination, and neurodegeneration around the ependymal region during canalicular syringomyelia development, the spatiotemporal pathological alterations have not yet been thoroughly clarified.^{18,19} It was proposed that transcriptomic analyses of spinal cord tissues could objectively reveal the various molecular and cellular pathological events.^{20,21} The current study lays a prototypical foundation for remodeling the ependymal niche to magnify the endogenous repair potential in syringomyelia, explaining the internal mechanism of the “moniliform configuration” as an early reversible state. We want to establish a templated landscape depicting the dynamic spectrum in cellular phenotypes and molecular biomarkers during syringomyelia development and to identify the best targets for treatment.

RESULTS

Canalicular syringomyelia in a rat model induced by extradural compression

In our model, the canalicular syringomyelia could closely mimic the morphology of syringomyelia in the human clinical situation. MRI shows altered CSF circulation in the subarachnoid space after the operation (Figure S1A). At post-op 4 weeks, 82.1% of 112 rats had syringomyelia confirmed by the MRI scans in the experimental group.

Surgical procedures for syringomyelia induction

The T12-13 intervertebral space was carefully separated to expose the ligament flavum; aseptic cotton balls (0.75 mg per 100 g body weight) were then reshaped into a long strip and stuffed into the extradural space below the T13 lamina with a nerve micro-stripper. After the cotton strip was completely placed, the compressed dura mater (remains intact) could be observed while the CSF space was obstructed (Figure 1A). In the sham group, only the T12-13 interlaminar space was exposed without subsequent extradural compression with cotton strips.

A decompression operation was performed at the site of the previous operation. The T13 lamina was carefully ground with a high-speed microdrill until the cotton strip was completely exposed; it was carefully removed using micro-tweezers and -scissors to ensure the recirculation of the CSF, which could be observed under the transparent dura mater (Figure 1B).

Morphology feature of the syrinx

The shape of the syrinx is mostly moniliform type, which locates at the rostral CC of the compression site with a longitudinal length of 2–3 vertebral segments (Figures 1C–1F). Initially, the syringomyelia presented in a separated pattern from post-op 2 weeks later, and over time, the MRI showed a gradual decrease in internal separations until the ultimate transition to an expanded pattern at a later stage (Figure S1A).

Dynamic change of syrinx

At post-op 4 weeks, with the cumulative syringomyelia positive rate of 82.1% (92/112) on T2-weighted MRI in the experimental group, there was no syrinx induced in the sham group (0/18). At this time, for rats without induced syringomyelia visible on MRI, syrinx will not appear again later; in rats with induced syringomyelia, the syringomyelia remained stable gradually.

The syrinx size changed significantly before post-op 6 week and stabilized later in the experimental group. It was presumed to be the “progression period” before 6 weeks and the “stabilization period” after 6 weeks. To evaluate the enlargement rate of the syrinx quantitatively, we analyzed the changes in the diameter and area of the syrinx. Extradural compression could induce continuous syrinx enlargement over time (Figures 1I–1K), and the growth rate of the syrinx before post-op 6 weeks was faster than that after post-op 6 weeks. From post-op 2 to 4 weeks, the syrinx is mainly reflected in longitudinal expansion; from 4 to 6 weeks, transverse expansion gradually appears, and early decompression at post-op 4 weeks might prevent or even reverse the further deterioration of the CC expansion. It was suggested that our syringomyelia model induced by chronic extradural compression had good temporal stability and repeatability during the follow-up until 8 weeks after the operation.

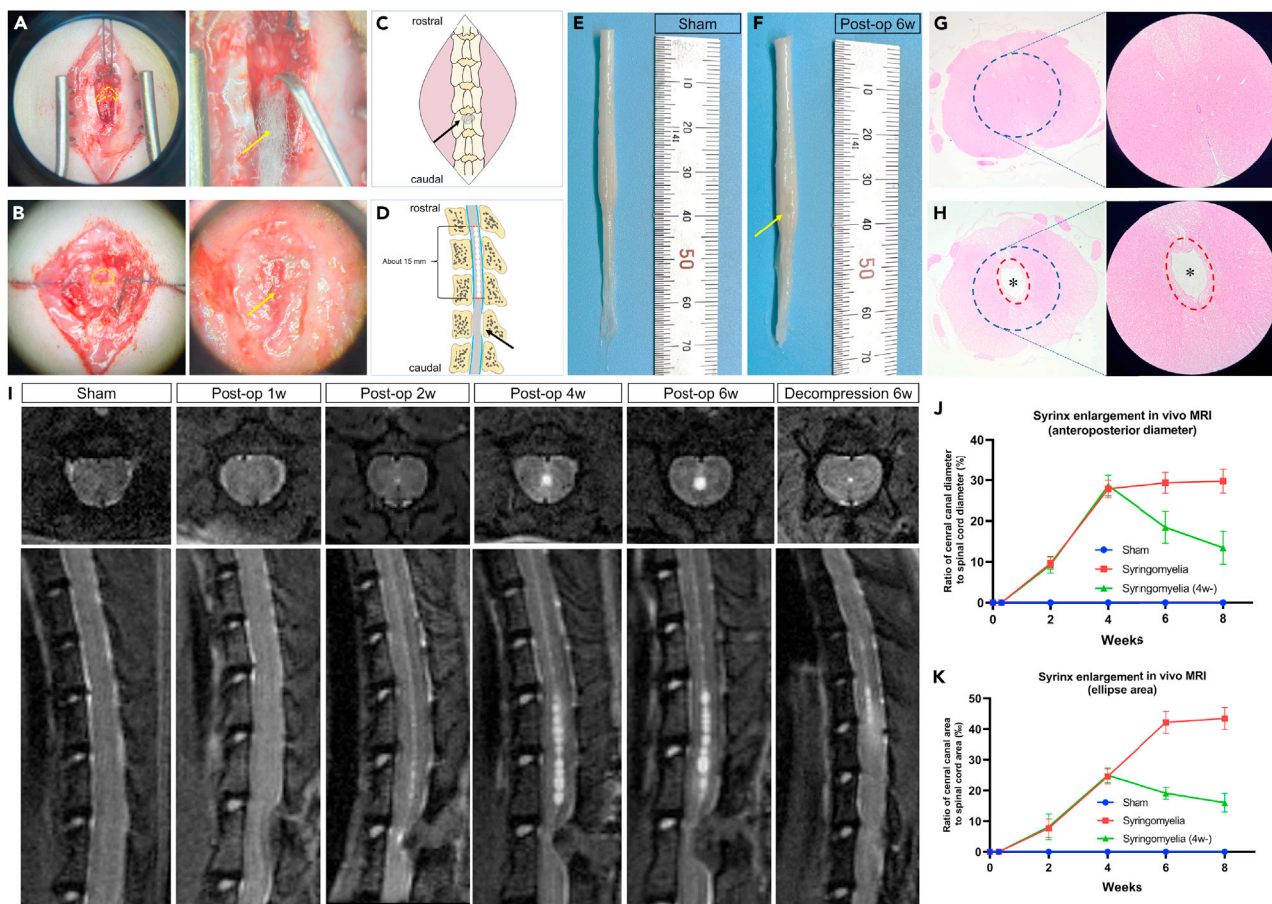


Figure 1. General characterizations of the Sprague-Dawley rat syringomyelia model

(A and B) A schematic illustration of the location of the epidural compression (A) and the anatomical positioning of the syringomyelia above the epidural compression site (B).

(C and D) Intraoperative presentations of the procedure for syringomyelia induction. The cotton strip was placed along the interlaminar space (area marked with yellow dotted lines) (C). Presentations of the decompression operation. The cotton strip was exposed (area surrounded by yellow dotted lines). After it was carefully removed, the yellow arrow showed blood vessels on the surface of the spinal cord (D).

(E and F) No obvious abnormalities were observed except for shallow indentations at the compression site (yellow arrow) in the experimental group.

(G and H) The whole and local magnification of the cross-sectional histological structure (HE staining) showed obvious edema around the expanded central canal in the experimental group compared with the sham group whose central canal was close to the recessive space.

(I) *In vivo* MRI and measurements of syrinx enlargement. Centered on the operation site, the sagittal and axial T2-weighted images were acquired.

(J and K) The syrinx size changed significantly before 6 weeks and stabilized after 6 weeks. However, early decompression at post-op 4w might prevent or even reverse the further deterioration of the CC expansion (4w-, decompression group).

After the operation, the ratio of the diameter of the syrinx (n) to the diameter of the spinal cord (m) increased significantly from 9.7 ± 1.5 at post-op 2w, 27.9 ± 2.2 at 4w, 29.4 ± 2.6 at 6w to 29.8 ± 2.9 at 8w (2 to 4 weeks, $p = 0.005$; 4 to 6 weeks, $p = 0.025$; 6 to 8 weeks, $p = 0.721$. Wilcoxon matched-pairs signed rank test). The ratio of the syrinx area (S1) to the spinal cord area (S2) increased from 7.7 ± 3.0 at post-op 2 weeks, 24.6 ± 2.5 at 4 weeks, 42.2 ± 3.6 at 6 weeks, 43.4 ± 3.5 at 8 weeks (2 to 4 weeks, $p = 0.005$; 4 to 6 weeks, $p = 0.005$; 6 to 8 weeks, $p = 0.012$. Wilcoxon matched-pairs signed rank test).

Behavioral and electrophysiological monitoring

A total of 130 rats were monitored for behavioral changes and for each time point more than 10 rats were analyzed.

BBB scores reveal no obvious locomotor deficits

BBB score was only slightly decreased to 18.0 ± 1.9 at post-op 1-day in the experimental group, but there was no significant difference compared with sham rats. At the post-op 6 weeks, BBB scores gradually restored close to a healthy level (21-score), indicating that our syringomyelia model has good safety without induced locomotor deficit during the long-term follow-up (Figure 2A).

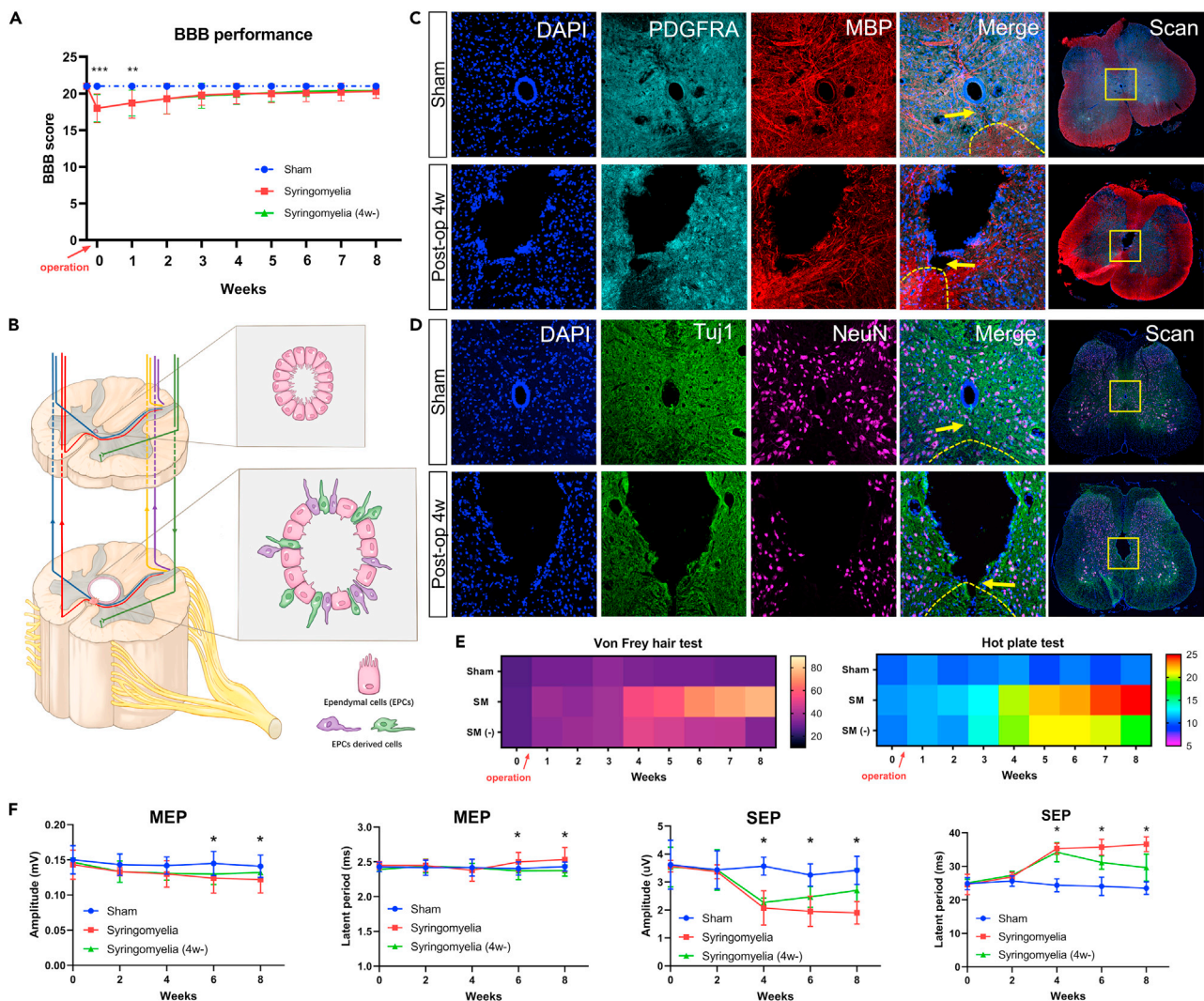


Figure 2. Secondary syringomyelia-related spinal cord injury and abnormal neurological symptoms

(A) BBB locomotor scores of the sham group and experimental group after induction of syringomyelia. During the follow-up period of 8 weeks, the BBB score shows that the motor function of the experimental group could recover spontaneously without treatment (** $p < 0.01$, *** $p < 0.001$).

(B) The schematic diagram of the syringomyelia-related central SCI. During the dilation of the central canal, cross-fibers located in the anterior symphysis of the central canal are the first to bear the brunt, and longitudinal conduction tracts away from the central canal, such as the corticospinal and spinothalamic tracts could survive.

(C) Immunofluorescence showed destruction of the cross-fibers (Tuj1) located in the anterior symphysis of the central canal and a decrease in the neuron (NeuN+) after post-op 4-week.

(D) Confocal views showed demyelination around the anterior symphysis region with diminishing MBP fluorescence intensity or even absence but a corresponding increase in OPCs (Pdgfra+).

(E) The Von Frey hair test and hot plate test showed a significant threshold elevation after post-op 4 weeks. As for the decompression SEP group (4w-), although the same transient threshold abnormality appeared at post-op 4-week, the sensory disorder seemed to gradually return to the normal level after decompression, or at least no longer progressed malignantly.

(F) According to the electrophysiological analysis by amplitude (AMP) and latency changes of motor-evoked potential (MEP), it was indicated that compared with the sham group, the rats in the experimental group began to show abnormalities after 6 weeks. In addition, the SEP showed an abnormality of both AMP and latency after 4 weeks ($n \geq 3$, * $p < 0.01$).

Electrophysiology analysis indicates secondary abnormalities

It was indicated that compared with the sham group, the rats in the experimental group began to show statistically significant abnormalities in motor-evoked potential after 6 weeks, which indicated secondary spinal cord injury (SCI) accompanied by further CC expansion. In addition, the somatosensory-evoked potential showed an abnormality in both amplitude and latency (Figure 2F).

Von Frey hair and hot plate test shows dissociative sensory disorder

Specifically, the Von Frey hair test and hot plate test showed a significant threshold elevation of superficial sensation in the hind paw after 4 weeks, corresponding to a certain superficial sensitivity deficit during syringomyelia formation. As for the decompression group, although the same transient threshold abnormality appeared at post-op 4 weeks, the sensory disorder seemed to gradually return to normal after decompression, or at least no longer progressed (Figure 2E).

Histopathological and ultrastructural investigation around the ependymal region

SEM showed that the cilia state was in dynamics from the overall distribution during syringomyelia development: the cilia decreased rapidly in the dilated area of the syrinx; however, cilia decreased slowly in the separation area. The distribution of cilia was not uniform at the same time point: the cilia density was significantly higher at the separation area than that at the area of syrinx dilatation. Besides, syringomyelia resolution was accompanied by the gradual recovery of cilia, especially at the separation area, with an increase in mitochondria-containing bulbs (Figures 3A–3D).

Transmission electron microscopy (TEM) revealed dynamic pathological changes around the ependymal region including loss of cell polarity, a decrease of microvilli and kinocilia in the apical cell cortex of the ependymal cells (EPCs), and destruction of tight junctions during the dilation of the CC. At post-op 6 weeks, complete disruption of cell junctions and change in cell polarity. However, after decompression, cell junctions are reestablished, and cell polarity restores with the relative recovery of cilia. The myelinated and unmyelinated axons are observed with severe tissue edema during the CC expansion. Axonal thinning, splitting, swelling, peeling, and degeneration in axoplasmic mitochondria are generally noted. The axons appear relatively healthy in the sham group. Those degenerative changes are coupled with the remyelination of baby axons, especially in the decompression group (Figures 3A–3D).

HE staining also indicated that edema was prominent around the CC during syringomyelia formation (Figures 1G and 1H). Corresponding to the neurological impairment characterized by segmental dissociative sensory abnormality, immunofluorescence (IF) showed destruction of the cross-fibers in the anterior symphysis of the CC and a decrease in neurons (NeuN⁺) of the pericentral parenchyma after post-op 4 weeks (Figures 2C and 2D). The number of GFAP⁺ cells within the CC and GFAP immunoreactive cells lying outside the EPC layer increased during the CC expansion (Figure 3E). The activated microglia (CD68⁺) were mainly distributed around the CC as an inflammatory response to the central SCI.

Bulk RNA-seq reflected the overall transcriptomic changes

Spinal cord tissues (15 mm in length) encompassing the syrinx segments were dissected and subjected to bulk RNA-seq (Figure S2A). The volcano map showed differentially expressed genes (DEGs) between the sham group and the experimental group at different time points (Figure S2B). Gene Ontology (GO) enrichment analysis was conducted with Metascape and visualized by Cytoscape, which revealed four modules involved in various biological processes enriched from DEGs (Figure S2C). In addition, it appeared that a temporal signature was evident, indicating that certain pathological processes occurred at distinct post-op time points.

Single-cell RNA-seq demonstrated the dynamic changes in cell subtypes

Although major alterations of temporal pathological events could be reflected objectively by the transcriptomic bulk data, the specific changes in cell subtype could be masked through bulk RNA-seq. To get around this, we performed high-throughput single-cell RNA-seq.

Based on the expression of cell-type-specific marker genes, 11 cell types were identified from a total of 82,862 sequenced cells (Figures 4A–4D). Additionally provided were single-cell RNA-seq results for particular time points (Figure 4E). In this study, we concentrated on EPCs, macrophages, microglia, oligodendrocyte progenitor cells (OPC), and oligodendrocytes separately extracted and re-integrated to delineate new cell subtypes. We also showed the dynamic changes in both gene expression and the proportion of each cell subtype at different time points. The most dynamically changing cell types are located in EPCs.

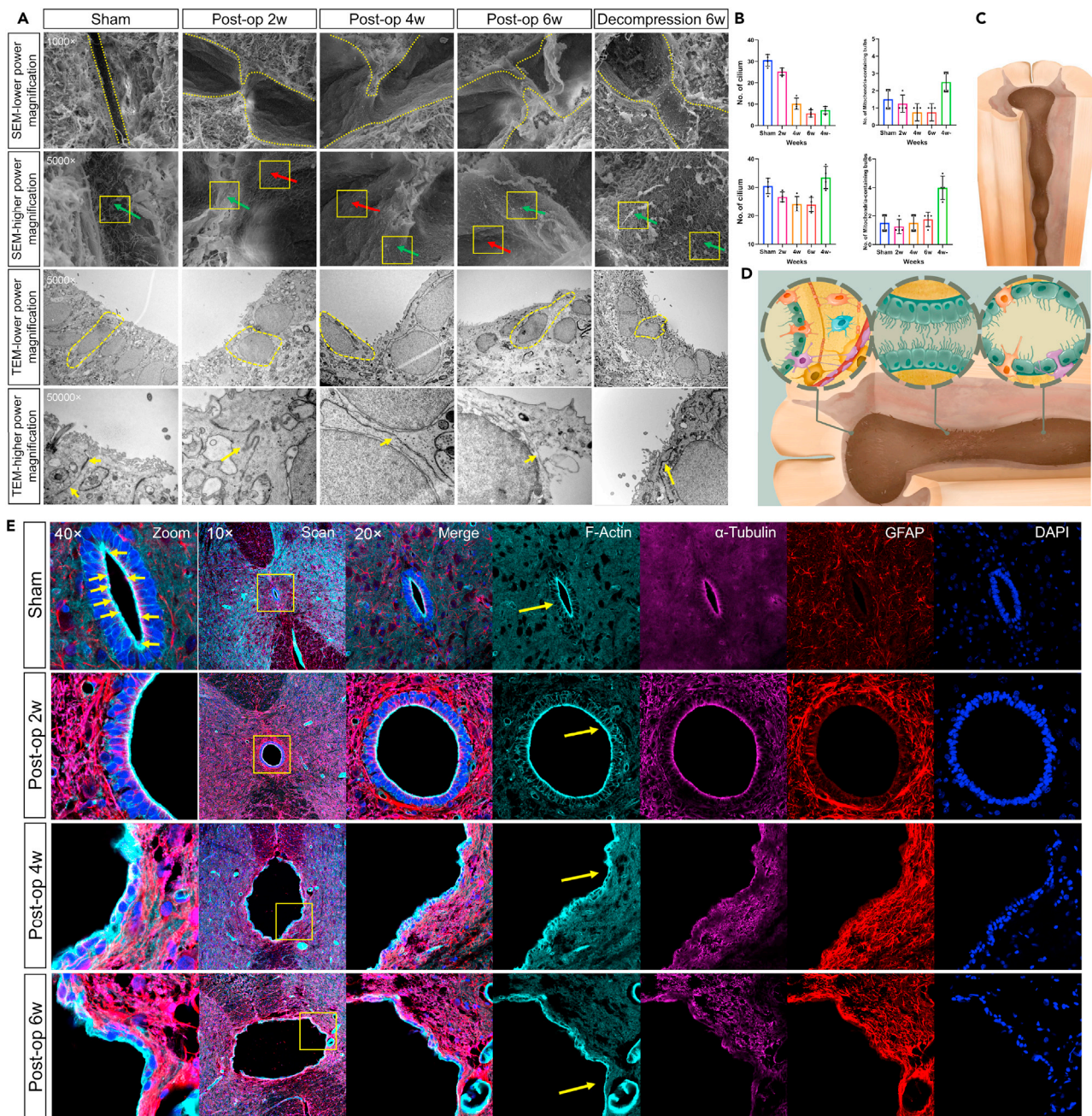


Figure 3. Ultrastructural investigation around the ependymal region

(A and B) Scanning electron micrographs (SEM) and transmission electron micrographs (TEM) of the spinal cord during the dilatation of the CC at low (top column, $\times 5,000$ to $\times 10,000$) and high (bottom column $\times 10,000$ to $\times 50,000$) power magnifications. Syringomyelia resolution was accompanied by the gradual recovery of cilia, especially at the separation area, with an increase in mitochondria-containing bulbs as well. (A) At post-op 6 weeks, complete disruption of cell junctions and change in cell polarity. However, after decompression, cell junctions are reestablished and cell polarity restores with the relative recovery of cilia. The myelinated and unmyelinated axons are observed with severe tissue edema during the central canal expansion (B). (C and D) The schematic illustration showed that the dilatation of the central canal (syringomyelia) presented in a moniform shape. (E) Confocal images indicate the immunostaining of the cytoskeleton around the CC. Cytoskeleton pattern rearrangements paralleled by ultrastructural modifications of the apical domain of ependymal cells were observed during the CC expansion. The Actin and microtubule structures (α -tubulin) become gradually disorganized. A high-magnification confocal image of a non-polarized ependymal cell is shown, and both polygonal and oval-shaped cells are shown in the encircled area. The number of GFAP-expressing cells within the CC and GFAP immunoreactive cells lying outside the ependymal cell layer (presumable but not active astrocytes) increased.

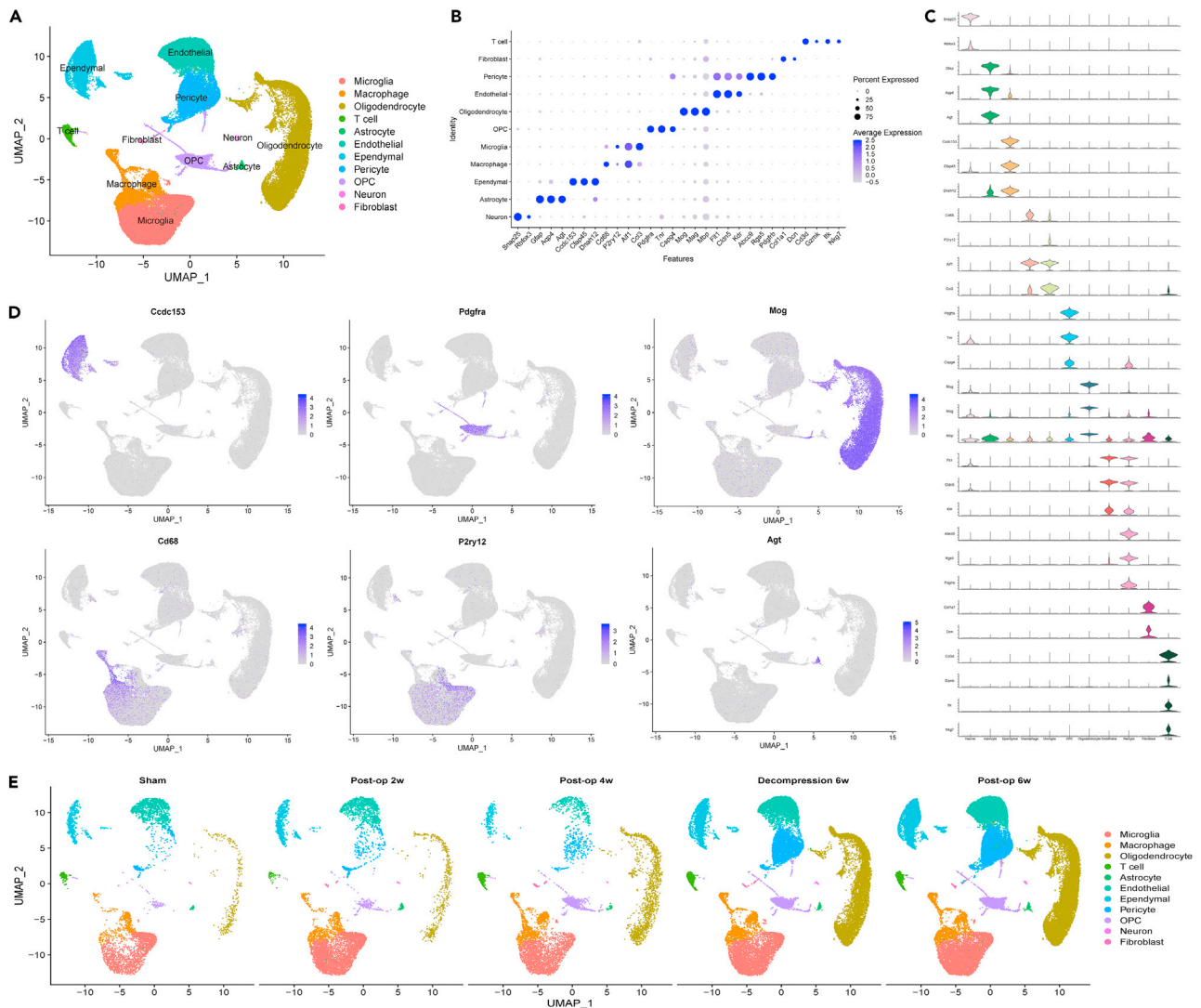


Figure 4. Single-cell RNA-seq landscape during syringomyelia development

(A) UMAP visualization plot of 82,862 cells sequenced from all samples, 11 cell types were defined based on the expression of cell type signature genes. (B) Dot plot of highest DEGs for each major cell type. (C) Violin plots showing the expression of the signature genes for each cell type. (D) UMAP of the expression pattern of the DEGs that best identifies several cell types. (E) UMAP plots indicate temporal changes of 11 cell types (E).

Dynamic changes of the ependymal subtypes during central canal expansion

We performed further subtype analysis of the EPCs, the UMAP of which revealed notable temporal changes during syrinx formation and resolution (Figures 5A and 5B). In general, EPCs showed high expression of EPC-specific marker genes such as *Foxj1* and *Ccdc153* (Figures 4G and 5C). To assess the heterogeneity of the EPCs, we identified two main distinct subtypes that were identified based on annotated marker genes, the motor ciliary ependymal subpopulations (with featured genes of *Cfap44* and *Sncg*), and the glial ependymal subpopulations (with a higher expression of *GFAP* and *Rnd3*) (Figure 5D). We plotted the expression of their marker genes. The different ependymal subpopulations showed different enrichment results according to their respective specific gene markers and displayed obvious differences in top DEGs (Figure 5H). In addition to the above two major subtypes, there appears to be a transitional state of EPCs that maintains relatively common characteristics in a primitive state of differentiation. We named them the primitive ependymal. In addition, there was also a cluster of cells that were proliferating with high

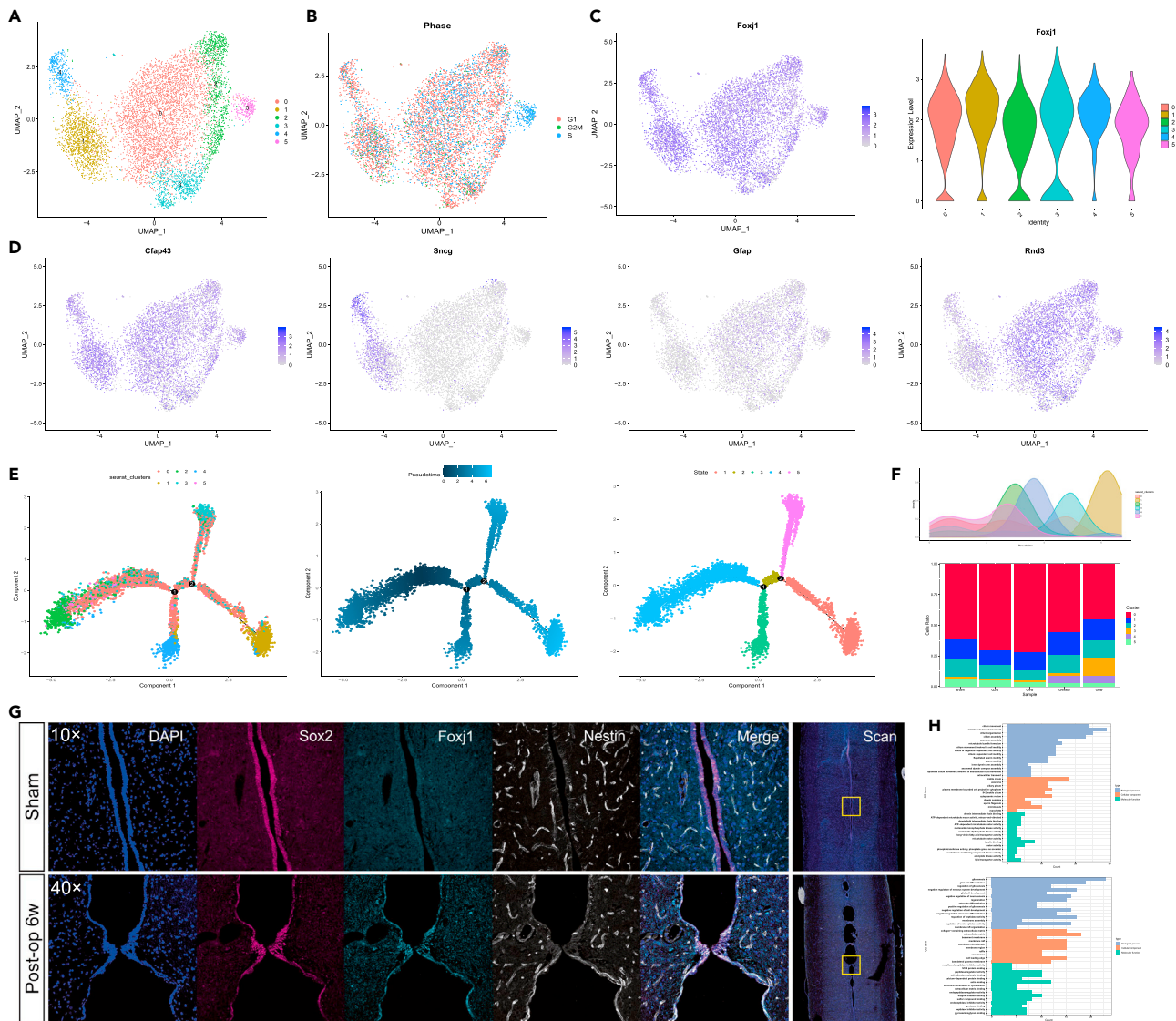


Figure 5. Dynamic changes in spinal cord ependymal populations post-op for syringomyelia

(A–D) We performed further subtype analysis of the EPCs, the UMAP of which revealed two main distinct subtypes. Subtypes were annotated using a combination of canonical markers, transcription factor expression, and GO enrichment analyses of the DEGs (A). Cell cycle assignment showed that cells in Cluster 5 were mainly in the S phase (B). In general, ependymal cells showed high expression of the EPC-specific marker Foxj1 in the dot plot and violin plot (C). Cells are colored by the expression value of canonical marker genes, the motor ciliary ependymal subpopulations (with featured genes of Cfap43 and Sncg), and the glial ependymal subpopulations (with a higher expression of GFAP and Rnd3). Values are log-transformed normalized expression counts (D). (E, F, and H) The differentiation and development trajectory of EPCs was constructed by the diffusion map of pseudotime analysis. Pseudotime trajectory analysis corresponding to the differentiation of EPCs from Cluster 0 to other clusters. Cluster 5 (proliferating) between Cluster 0 in the early state and the other clusters. Cells are colored by cell types, pseudotime, and cell states, as indicated, from the left to the right panels (E). A ridge plot was drawn based on the pseudotime analysis to simulate the trajectory of cell clusters in cell differentiation and the proportions of ependymal-lineage subtypes at each time point from the top to the bottom (F). GO biological process terms associated with the top DEGs among two different cell subtypes (H). (G) Immunofluorescence shows the expression pattern of Sox2, Foxj1, and Nestin during syringomyelia development. EPCs (Foxj1+) in the CC area represented the EPCs with colocalization of Sox2 and Nestin. During the syringomyelia formation with the CC expansion, the syringomyelia was in a moniliform shape, and there were obvious separations between adjacent dilated compartments. The EPCs are irregularly distributed throughout the central canal due to moniliform-like dilatation. The stacked cells remained as EPCs (Foxj1+) in the stenosis, resembling a tunneling effect and showing that the CC was still communicating, but the monolayer of cells was organized in the significant dilated area and even disrupted in some regions. The cytoskeleton outlined by Nestin also became gradually disorganized or even disordered at post-op 6 weeks.

expression of *Ki67*, *Top2a*, and *Mcm5*. Cell cycle assignment showed that cells in Cluster 5 were mainly in the S phase (Figure 5B).

The differentiation and development trajectory of EPCs was constructed by the diffusion map of pseudo-time analysis, which captures the EPCs along four divergent branches projected onto the principal curve (Figure 5E). It could be seen that four main branches were centered on Cluster 0, originating from state 2 with two nodes of different cell states, which also correspond to the judgment of differentiation to two different cell subtypes. Pseudotime trajectory analysis corresponding to the differentiation of EPCs from Cluster 0 to other clusters (Figure 5F). Cluster 5 (proliferating) between Cluster 0 in the early state and the other clusters. Cells are colored by cell type, pseudotime, and cell state, as indicated, from the left to the right panels (Figure 5E).

Confocal analysis of longitude-sectioned spinal cord tissue showed the typical moniliform-like syringomyelia with central canal EPCs (*Foxj1* and *Sox2* co-expression), and the obvious change in cell arrangement during central canal expansion, accompanied by changes in the cytoskeleton outlined by Nestin (Figure 5G).

Although reactive astrocytes have traditionally been associated with gliosis, increasing data suggest that ependymal-derived cells also play a significant role in the formation of the glial scar.^{22,23} The top biological processes for Astro-ependymal cells (Cluster 2 and 3) were related to glial cell development, differentiation, and migration. Cluster 2 is defined by processes related to the regulation of peptidase activity, whereas Cluster 3 is defined by lipid transport.

The motile ciliary ependymal subpopulation displayed unique features and notable temporal changes. Cluster 1 is a highly specialized subtype of motile ciliary EPCs, the proportion of which gradually increased during syrinx development, especially after decompression.

EPC Cluster 1 was extracted to facilitate the description of dynamic changes in cilia-related gene expression levels at different time points. First, the DEGs were derived at different time points from EPC cluster 1 during syringomyelia progression, and GO enrichment analysis was performed to obtain the terms associated with cilia motility, maintenance, assembly, or disassembly (Figures 6A and 6B). At post-op 2 weeks, “response to fluid shear stress” and “the negative regulation of actin-based cell projection” appear, while at post-op 4 weeks, the “negative regulation of actin filament-based movement” gradually appears. At post-op 6 weeks, “the negative regulation of biological process” and “actin-related assembly or organization” exist simultaneously and conflict with each other. The relative increase in the number of cells in Cluster 1 was accompanied by negative regulation of actin proteins. As a possible reaction to the loss of cilia during syrinx formation, this may reflect a homeostatic strategy per se.

With the emergence of a new cilia-related subtype (Cluster 4) at post-op 6 weeks, we compared EPC Cluster 4 with Cluster 1, and genes such as *Sncg*, *Tagln*, and *Fmod* were upregulated, implying an association with the enhanced cytoskeleton (actin and microtubules) and restoration of cellular junction (tight junction) at the transcriptional level (Figure 6D). The enrichment results for DEGs revealed it is associated with the positive regulation of EPC migration, rearrangement, and adhesion, so we speculated that Cluster 4 might be associated with “wound healing” (Figure 6E).

By confocal analyses, Actin staining is shown as a patchy brilliant ring bordered by a less intense zone in the radial characteristic of delineating polarized EPCs that comprise the CC in the sham group. Actin pattern rearrangements were identified, which were accompanied by subtle ultrastructural modifications of the apical region of EPCs during the CC expansion. The non-polarized EPCs in high-magnification views are exhibited with both polygonal and oval-shaped cells outlining in the encircled area. Cytoskeletal alterations were accompanied by a decrease in centrioles as well as cilia (Figure 3E).

The heterogeneity and potential lineage relationships between EPCs and oligodendrocytes

All macroglial cells including EPCs, astrocytes, OPCs, and oligodendrocytes were extracted, reclustered, and re-embedded in a new UMAP plot (Figures 7A and 7B). The oligodendrocyte lineage cells (*Sox10*) formed predicted clusters that exhibited a temporal transition from OPCs through preoligodendrocytes to mature oligodendrocytes. OPCs expressed canonical genes such as *Tnr*, *Cspg4*, and *Pdgfra*. We then

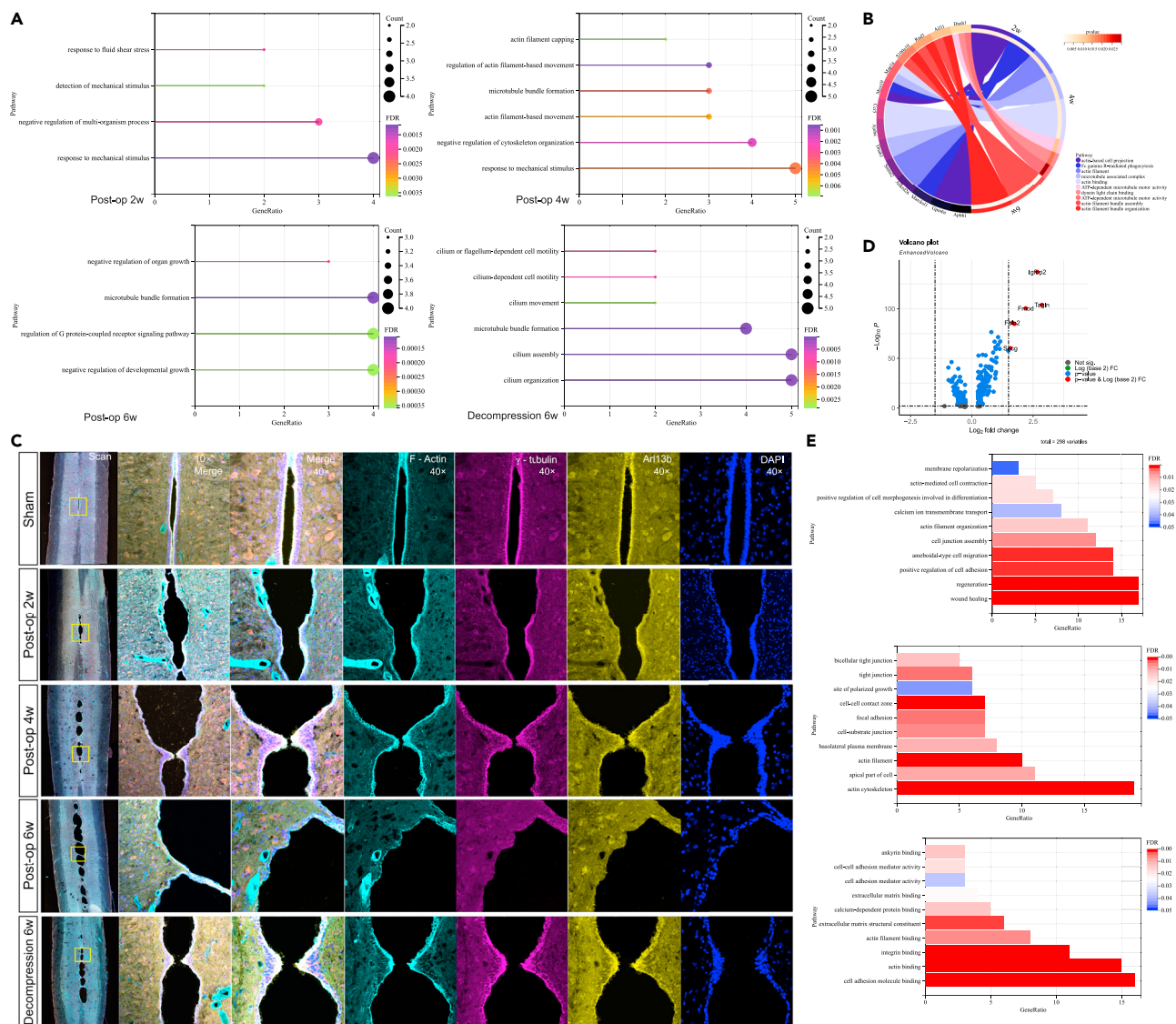


Figure 6. Confocal images showed the dynamic changes of the ependymal cytoskeleton proteins

(A and B) The DEGs were derived from EPC cluster 1 at different time points during syringomyelia progression, and GO enrichment analysis was performed to obtain the temporal terms associated with cilia motility, maintenance, assembly, or disassembly, matching results with immunofluorescence counterparts. The GO enrichment for upregulated DEGs is presented through a dot-line plot (A and B), and for downregulated DEGs presenting through the Sankey diagram.

(C) Confocal images showed the syringa expanded sharply from post-op 2 to 6 weeks in moniliform shape, and the decrease in cilia was gradually aggravated. Cytoskeletal alterations (F-Actin) were accompanied by a decrease in centrioles (γ -tubulin) as well as cilia (Arl13b) during syringomyelia development. At the post-op 6 weeks in the syringomyelia group, both cell polarity and cilia were abnormally arranged, and no syringa shrinkage was observed. At post-op 6 weeks in the syringomyelia group, abnormal cytoskeleton with a complete change in cell polarity, in concert with disappearing centrioles and few cilia. At the post-op 6 weeks in the decompression group, the EPC polarity and cilia have recovered in some regions. From the temporal sequence, it appears that the loss of cilia promotes the development of syringomyelia. The maintenance of cilia in some spatial areas, especially after decompression.

(D and E) EPC Cluster 4 compared with cluster 1, the genes such as *sneg*, *tagln*, and *fmod* were upregulated, implying an association with the enhanced cytoskeleton (actin and microtubules) and restoration of cellular junction (tight junction), (D) and the enrichment results for DEGs revealed an association with positive regulation of EPC migration, rearrangement, and adhesion (E).

identified two main OPC clusters (OPC-A and -B) that displayed distinct molecular features. Whereas OPC-A were present in abundance at all time points, likely representing prototypical OPCs, OPC-B appeared only in a later stage, with numbers peaking at post-op 6 weeks but decreasing significantly after decompression. OPC-B was identified from OPC-A by its higher expression of *Sox9*, *Ccdc113*, and

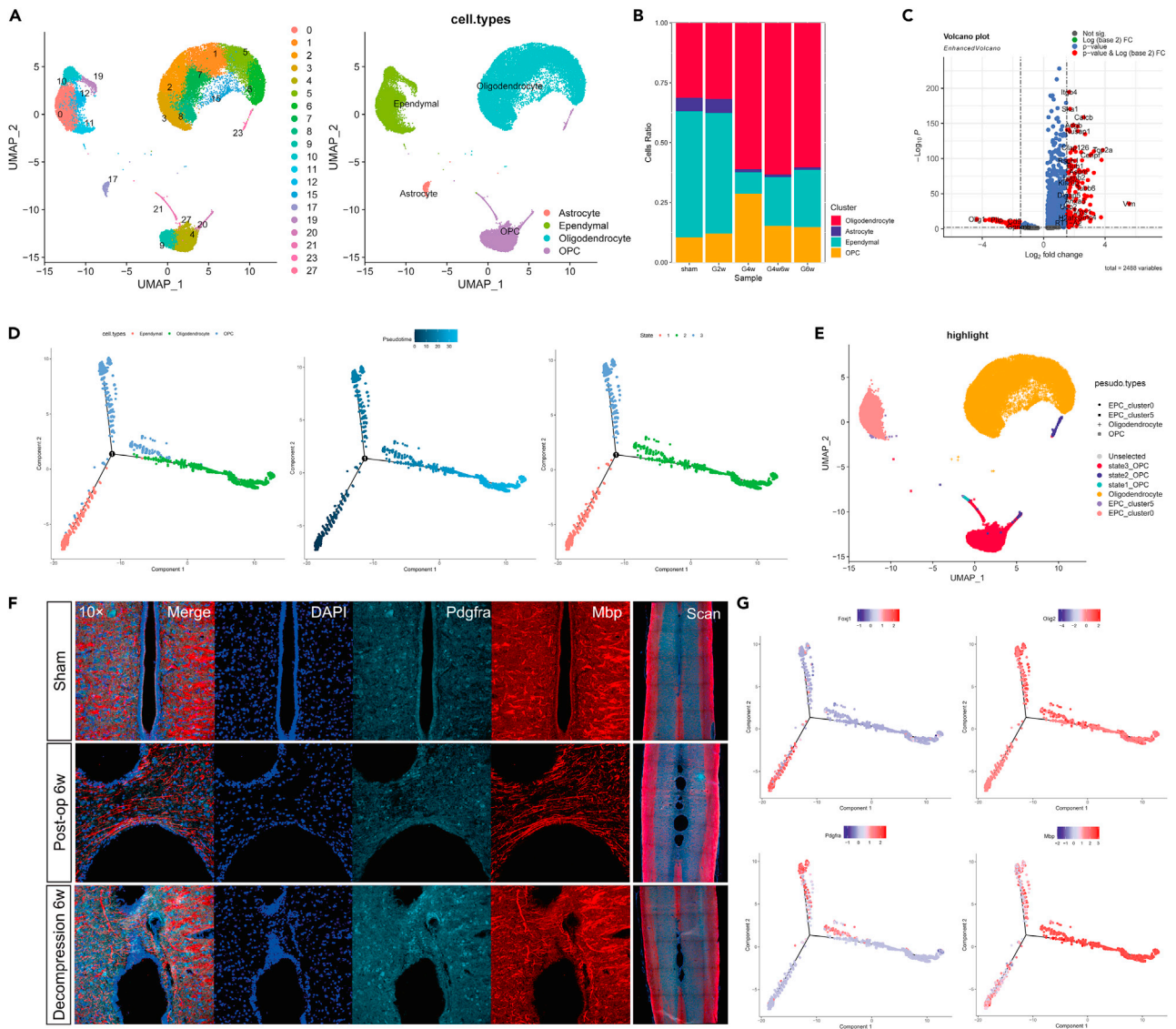


Figure 7. The heterogeneity and potential lineage relationships between ependymal and oligodendrocyte lineage

(A and B) UMAP plot of all macroglial cells. Ependymal cells, astrocytes, oligodendrocyte progenitor cells (OPCs), and oligodendrocytes were extracted, reclustered, and re-embedded in new UMAP coordinates (A) The bar diagram shows the proportion of each cell subgroup (B).

(C) We compared the OPC-A (OPC in state 1) and the prototypical OPC-B (OPC in state 3) that displayed distinct temporal and molecular features.

Significantly upregulated and downregulated genes are shown as orange and green dots, respectively.

(D) Pseudotime trajectory analysis corresponds to the differentiation from EPCs in the early state to OPC to oligodendrocytes. Cells are colored by cell types, pseudotime, and cell states, as indicated, from the left to the right panels.

(E) We re-embedded the cells into the UMAP map according to the different states obtained from the pseudotime trajectory analysis and found that OPC-state 1 is located at OPC-cluster 21, while OPC-state 2 is located at OPC-cluster 23. Therefore, it is speculated that cluster 21 seems to be the transition subpopulation from EPC to OPC, while cluster 23 is the transition state from OPC to oligodendrocytes.

(F) Since graded expression based on fluorescence intensity is difficult to quantify using immunohistochemistry, we could find that the OPC (Pdgfra+) distributed around the cavity expansion as well as the MBP fluorescence intensity gradually became fainter or even interrupted with the central canal expansion, but the intensity of MBP recovered significantly in decompression group.

(G) Expression of ependymal and oligodendrocyte lineage genes defining each branch. Annotated gene markers for ependymal and oligodendrocyte lineage stages projected onto the diffusion map principal curve show stepwise ependymal oligodendrogenesis and the continuous transition from OPC to oligodendrocytes.

Cfap44 and lower expression levels of *Sox10*, *Olig1*, and *Olig2*, which indicated the shared similarity with ependymal lineage cells in transcription factor expression (Figure 7C). GO analysis of DEGs between OPC-A and -B showed biological processes associated with “positive regulation of neuron projection development” and “neuron differentiation” in OPC-A, and “cell division” and “proliferation” in OPC-B.

Finally, it is interesting to note that OPC-B had several lineage features in common with ependymal subtypes (Cluster 0, 5) representing an early stage in the diffusion map of pseudotime analysis (Figure 7D). In addition, pseudotime trajectory analysis corresponds to the transition from EPCs through OPCs to oligodendrocytes (Figures 7E–7G). Our findings show the heterogeneity and potential lineage links between EPCs and OPCs that reflect the influence of CC enlargement on their differentiation state, with OPC-B appearing to be close to a transition state.

Microglia cells coordinate between neuroinflammatory responses and SCI recovery

We re-integrated macrophages and microglia cells to better understand myeloid cell heterogeneity, as characterized by their annotated marker gene expression (*CD63*)²⁴ (Figure 8A). The UMAP's overall structure indicated two major subpopulations related to central nervous system microglia and peripherally derived myeloid cells, which demonstrated predicted expression patterns between microglia and macrophages: *P2ry12* and *Tmem119* appeared to be the classic microglial markers in contrast to macrophages, while macrophages were noted by the relative downregulation of microglia canonical cell marker genes (Figure 8B).

We further identified five microglial subtypes. Homeostatic microglia (Cluster 2) were identified based on the higher expression of the annotated marker *P2ry12* in a steady state.²⁵ The other four non-homeostatic microglia subtypes were labeled chemotaxis-inducing, inflammatory, disease-associated, and dividing microglia, respectively, based on their GO terms for biological processes (Figure 8E).

It could be characterized by the preferential expression of heme oxygenase *Ccl2* in chemotaxis-inducing microglia and *C3* and *NF-κB* family in inflammatory microglia. GO terms for chemotaxis-inducing microglia, which represented the first responding non-homeostatic subtype, were associated with cell adhesion, migration, and motility. The higher expression of the inflammatory complement-related genes in microglia corresponded to GO terms associated with phagocytosis and leukocyte activation in inflammation (Figure 8E). Genes associated with the cell death terms were not self-death pathways, but rather mostly cell apoptosis-related with inflammation response (*NF-κB*). Disease-associated microglia (DAM) had a low level of *P2ry12* but a high level of *Igf1*. DAMs were distinguished by preferential expression of the purinergic receptor *ApoE*, *Gpnmb*, and increased co-expression of *CD68* (Figure 8B). GO terms for this special subtype were mostly associated with antigen processing and presentation, and negative regulation of cell activation (symbiotic process) (Figure 8E). Dividing microglia expressed high levels of cell division-related genes such as *Ki67* and *Top2a*. GO terms for dividing microglia were mostly related to the cell cycle and regulation of nuclear division. To validate the distribution of the activated microglia *in vivo*, we performed IF using antibodies against *CD68* and *Iba1* to spatially validate our results. While *CD68*⁺ cells were not present in the sham group, *CD68*⁺ cells started to appear during syrinx formation. Therefore, IF data support the molecular identification of DAM and their temporal progression during syringomyelia development *in vivo* (Figures 8C and 8D).

DISCUSSION

Previous studies have proposed several pathophysiologic mechanisms that contribute to the development of syringomyelia, with various possible predisposing hypotheses.^{1,6} It is widely assumed that its pathogenesis centers on subsequent disruption of CSF circulation originating in obstruction of the subarachnoid channels caused by intraspinal obstructive lesions, which are usually visible during surgical exposure.^{4,5,7} Once the primary disease occurs, the imbalance of CSF exchange between the CC and subarachnoid space with abnormal accumulation of CSF, in turn, leads to persistent dilatation of the CC. It eventually evolved into a series of chronic clinical manifestations unique to secondary central SCI.²⁶ Patients are usually plagued by segmental sensory paresthesia or dissociation, and some may experience weakness of limbs and muscle atrophy. Moreover, the wall of the syrinx away from the primary lesion is formed by CC remnants consisting astrocytic branches or flattened EPCs lacking normal polarity.³ Therefore, canicular syringomyelia is closer to hydromyelia, which is similar to subacute or chronic non-communicating hydrocephalus.²⁷

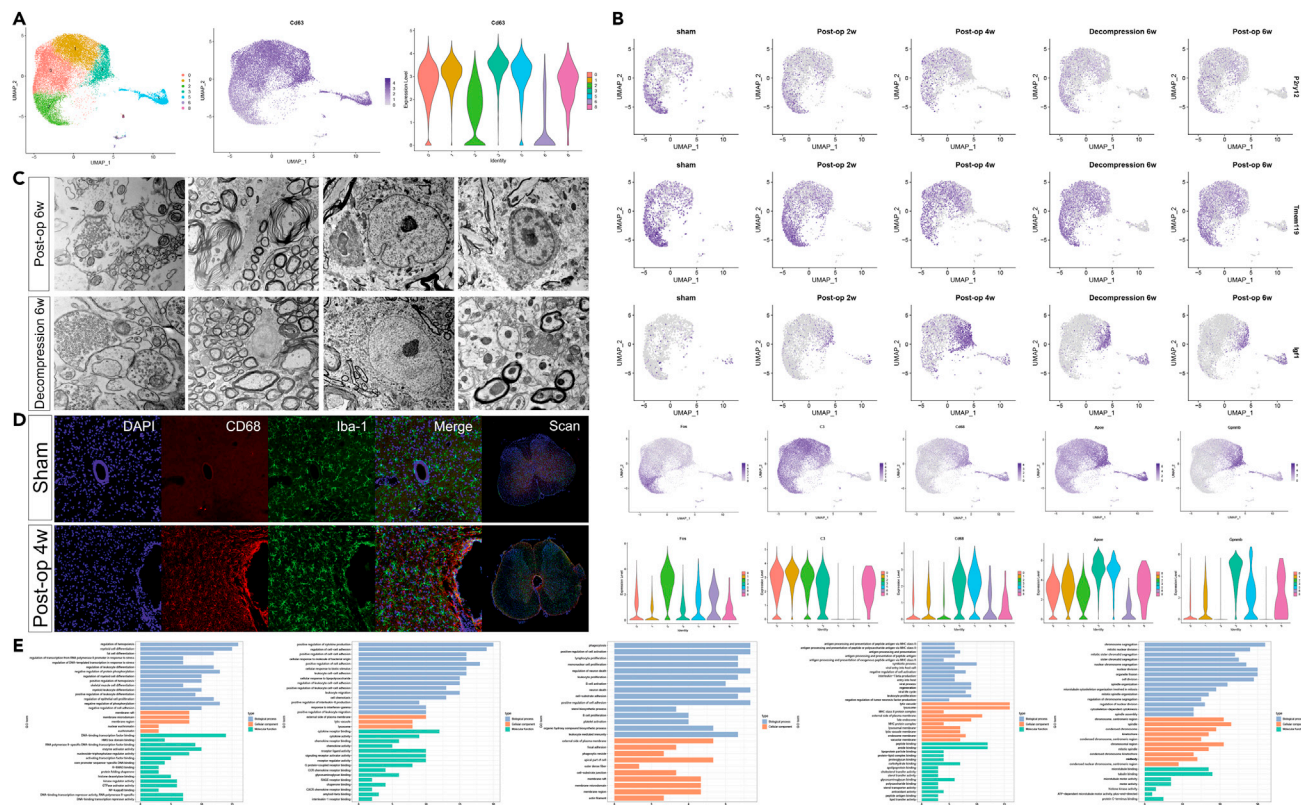


Figure 8. Molecular and temporal profile of microglia and macrophage subtype heterogeneity after syringomyelia induction

(A) We re-integrated microglia and macrophages as identified by their annotated marker gene expression (CD63). The overall structure of the UMAP revealed two major subpopulations corresponding to central nervous system microglia and peripherally derived myeloid cells (A) P2ry12 and Tmem119 seemed to be the canonical microglial markers. Macrophages were identified by the reduced expression of microglial cell markers.

(B and E) We identified 5 microglial subtypes. (B) Homeostatic microglia (Cluster 2) in the regulation of hemopoiesis and response to stress were identified based on its expression of several annotated markers of steady-state microglia, such as P2ry12 and Tmem119. (B) UMAP of the expression pattern of several annotated gene markers split by different time points into the top three columns. Cells are colored by neighborhood density in UMAP space to illustrate shifts over time. (B) UMAP of the expression pattern of some DEGs that best identifies each cell type. Darker blue colors indicate higher expression density in the UMAP. Values indicated are lognormalized counts per cell. (B) The other 4 non-homeostatic microglia subtypes were labeled chemotaxis-inducing, inflammatory, disease-associated microglia, and dividing microglia respectively, based on their gene ontology (GO) terms for biological processes (E).

(C) Ultrastructural investigation of the parenchyma of the spinal cord around the ependymal region. The degenerative changes are coupled with the remyelination of baby axons. The axons appear relatively healthy with normal synaptic structure, including dense synaptic granules indicating that regenerated myelin whose myelin lamellae were thin but tight with mitochondria increase, which was more common in the decompression group. Microglia are visible around the disrupted myelin sheath.

(D) Confocal images showed the distribution of the microglia *in vivo* using antibodies against CD68⁺ and Iba1 to spatially validate our results. While CD68⁺ cells were not present in the sham group, CD68⁺ cells started to appear during syrinx formation. The activated microglia (CD68⁺) were mainly distributed around the central canal as a response to the central SCI (D).

The specific pathophysiological mechanism remains unclear for subsequent CC expansion. After an initial cyst is formed, hydrodynamic factors are likely to play a role in delayed syrinx development.²⁸ It might be challenging to identify the origin of the syringomyelia, let alone take steps to prevent early primary neurological deficits.²⁹ However, it would be beneficial if we could minimize the aggressive progression of syringomyelia and prevent secondary SCI. That means capturing the key pathological factors during syrinx development is of great importance.

Clinically, compression injuries are becoming more common, and numerous efforts at animal model replication indicative of the specific clinical cases have been documented in the literature.³⁰ For previous syringomyelia animal models,^{31–33} the commonality lies mainly in that CC could expand as a result of increased turbulence that prompted CSF flow to the CC through the perivascular spaces (Virchow-Robin space). At this point, it seems to be consistent with the effect of our animal model. As one of the compression models

for syringomyelia research, our model with extradural compression to block CSF flow did not involve disruption of the dura mater. Compared with rigid substances such as plastic pipe, cotton has good plasticity and can be reshaped according to the epidural space during the stuffing process so that the subarachnoid space is more thoroughly blocked; furthermore, injury to the spinal cord is less likely.

Based on our previous reproducible animal model of canalicular syringomyelia by the extradural microoperation with good reversibility to closely mimic the clinical situation in humans,¹⁵ it is necessary to track and clarify the temporal and spatial pathological process of secondary SCI during the development of canalicular syringomyelia.

The polarized EPCs surround the CC, with an apical compartment contacting the lumen and a lateral surface connecting the neighboring cells and the extracellular matrix.³⁴ Moreover, planar polarity mechanisms make sure the orientation of all EPCs' apical and basal domains is in the same direction, and the normal intercellular communication, which coordinated beatings of multiple motile cilia with synchronized orientation, generates directional fluid flow on the tissue surface.³⁵ The pioneering study revealed that the anatomical and functional integrity of the CC is intimately linked to the integrity of the cytoskeleton of the multiple cells lining its lumen,³⁶ which is therefore closely related to the maintenance of normal CSF circulation and the balance of parenchymal microenvironment by coordinating the cilia oscillations.³⁷

According to our results, during the CC expansion, abnormal cell polarity was seen in the ependymal region as well as loss of motile cilia and disruption of tight or gap junction. Not only does that present a gradient temporal dynamic change but abnormalities also show obvious uneven spatial distribution. The CC expands dynamically, accompanied by obvious pathological changes in the spinal cord parenchyma, which is relatively chronic, concentrated on the ependymal region, and belongs to a type of central SCI.

Based on our results, the syrinx expanded sharply from post-op 2 to 6 weeks, and the decrease in cilia was gradually aggravated. In the meantime, tissue edema gradually appeared with obvious demyelination around the CC, in presence of progressive destruction of axons and neuronal degeneration in spinal cord parenchyma. At the post-op 6 weeks in the syringomyelia group, both cell polarity and cilia were abnormally arranged, and no syrinx shrinkage or SCI recovery was observed. At this point, endogenous repair in the ependymal region seems to be impossible to compensate for the injury, indicating a poor outcome. At the post-op 6 weeks in the decompression group, although the ependymal cell polarity and cilia did not convert to normal, they kept relatively normal in some regions. At the same time, the syrinx was resolved, and the spinal cord parenchymal injury gradually recovers. Self-repair gradually compensates for the injury with myelin regeneration, and it finally tends to a better outcome with obvious neurological function recovery. Overall, from the temporal sequence, it appears that the loss of cilia promotes the development of syringomyelia. However, the surviving cilia in separation seem to be crucial for the syringomyelia resolution after decompression.

As for pathological changes around the EPC region during CC dilation, the number of GFAP-expressing cells within the CC (the increased production of GFAP by EPCs) and GFAP immunoreactive cells lying outside the ependymal cell layer (presumable but not active astrocytes) increased during CC dilation. GFAP, a protein that belongs to intermediate filaments and which is typically abundant in astrocytes, serves as the main constituent of the fibrous matrix.³⁸ GFAP in the ependymal region could be regulated by injury-induced expression in resident EPCs as well as glial cell infiltration.³⁹ By interacting with the extracellular matrix, GFAP can modulate important cellular processes or molecular transcription mechanisms, such as proliferation, migration, differentiation, membrane transportation, and cell adhesion, increasing cell survival with stress tolerance.⁴⁰

Transcription factor (TF) enrichment analyses of the bulk-sequencing data objectively revealed the most significant TFs during syringomyelia development. A large part of TFs (potentially master control genes) is predominantly expressed in microglial cells, indicative of the critical roles of microglial cells during syringomyelia development. Microglia are activated dynamically during CC expansion. The expression of homeostatic genes gradually decreases while the chemotaxis-inducing and inflammatory-related clusters appear gradually with a temporal-sequence expression of *Igf1*, demonstrating that the inflammatory response does exist, which is consistent with the bulk data. However, inflammation does not seem to be as dramatic as

the stress in acute SCI. More interestingly, the subpopulation of the DAM could be distinguished by preferential expression of the purinergic receptor *ApoE* and *Gpnmb*,⁴¹ with a transcriptomic profile related to phagocytosis, autophagy, and mitochondrial metabolism, and to express genes related to the anti-inflammatory response alone. Confocal images showed the activated microglia (CD68⁺) were mainly distributed around the CC as a response to the central SCI during syrinx formation. The increased expression of *CD68* could be traced mainly at the DAMs. Even after decompression when parenchymal damage tended to ease down and CC stabilized, the microglial populations still deviated from those before the injury, indicative of long-lasting alterations in the immune microenvironment.

During syrinx development, EPCs keep self-regeneration (Figure S1B), and EPCs mainly differentiate into two different types (glial EPC and ciliated EPC). During the syringomyelia formation (post-op 2–6 weeks), the proportion of cilia-related EPCs (Cluster 1) gradually increased. In addition to cilia characteristics, Cluster 4 emerging at post-op 6 weeks was also associated with cell adhesion.⁹ Confocal images showed that at post-op 6 weeks in the syringomyelia group, abnormal cytoskeletons (F-Actin) and cell junctions were destroyed with a complete change in cell polarity, combined with disappearing centrioles (γ -tubulin) and few cilia (Arl13b) (Figure 6C). However, at the same time in the decompression group, abnormalities in ultrastructure were gradually restored compared with the syringomyelia group. Significantly, cilia density and mitochondria-containing bulbs increased in the syrinx separations (Figure 3A).

Actin, as another important cytoskeleton protein of the EPCs, plays an important role in maintaining cell polarity and protecting centrioles thus maintaining cilia motility.⁴² Plastic changes in the actin cytoskeleton are modulated by the coordinated activity of various actin regulators,⁴³ such as the increased detection of mechanical stimulus. When CSF disorders bring about the shear stress on cilia, the cilia dynein arm in charge of ciliary motility is disturbed,⁴⁴ disrupting the actin network; at the same time, disruption of cell polarity due to CC expansion could also affect the ciliary coordination and exacerbates actin disorder.⁴⁵ The combined factors drive the ciliary basal body (centrioles) shedding with cilia axoneme disassembling, which in turn leads to the syringomyelia progression (Figure 6C). This corresponds to the downregulation of actin or tubulin-related genes^{46,47} in Cluster 1. It seems there was some self-compensation for cilia shedding per se (dynamic changes in EPC subtypes and cilia-related genes of Cluster 1), so we hypothesize that only when the CSF obstruction resolved (decompression as a prerequisite), cilia would stop losing and even favor regeneration, as was seen in the differences between syringomyelia and decompression group (concurrent with parenchymal SCI recovery) at the post-op 6 weeks.

According to our results, we hypothesize that the abnormalities of EPCs are causally related to the disturbance of CSF circulation in the syringomyelia and the pathological changes in the spinal cord parenchyma as a vicious circle. On the one hand, the abnormality of ependymal cell polarity with motile cilia damage might reflect the unrestricted expansion of the CC accompanied by the continued progression of parenchymal edema, which ultimately ended in the inability of endogenous repair to effectively compensate for the injury. On the other hand, the impaired CSF circulation and microenvironment in the spinal cord parenchyma aggravated the ependymal cell abnormality and cilia dysfunction. Although the organism shows some signs of self-recovery, there was no actual realization of self-reversed presentation.

However, effective decompression is a prerequisite for syringomyelia regression and injury recovery, and we speculate that effective decompression facilitates the CSF recirculation and improvement of pathological changes in the spinal cord, ultimately leading to functional recovery as a virtuous circle. On the one hand, after decompression, the retaining cilia could be observed at the syrinx separations with a relatively normal cellular polarity, which could help in promoting CSF circulation recovery, making that CC dilatation no longer exacerbated and SCI no longer progresses. That means endogenous repair gradually overwhelms the SCI so that the neurological function is restored. On the other hand, the improvement of pathological changes (parenchyma edema) after decompression might also feed back into syrinx ablation, just pending in-depth CSF flow studies.

The reason why cilia are difficult to be restored in the dilated area of the syringomyelia, especially without decompression, is speculated to be the severely altered cell polarity of the EPC, which leaves to the severe destruction of the actin protein skeleton. In addition, the actin protein skeleton is relatively well preserved in the septum likely conducive to cilia regeneration.⁴⁸ Therefore, based on effective decompression,

regulating the niche of EPC in the promotion of cytoskeleton remodeling and motile cilia recovery by certain adjuvant interventions may have far-reaching clinical significance in promoting CSF circulation, syringomyelia resolution, and the overall parenchyma microenvironment.

Spinal cord damage has a degree of self-regeneration,¹¹ and the central SCI associated with syrinx also possesses endogenous repair potential,^{27,28} mostly via OPCs and DAMs. Endogenous repair tends to gradually increase as the syringomyelia and cord injury worsen, but the more advanced the syringomyelia, the harder it is for endogenous repair to make up for the damage. Effective decompression in the early stage could prevent the syrinx from developing, avoiding further progression of the damage so that self-repair can completely compensate for the neurological injury, as can be seen from the results of the early decompression group compared with the natural progression group. After all, the damage caused by syrinx dilatation mainly centered on the EPC region, and it had a chronic progression with corresponding endogenous repair initiation.

Therefore, the release of CSF obstruction is a prerequisite for recovery from neurological function. If the CC is unrestrictedly dilated, it would lead to a progression of secondary injury and even more severe manifestations involving the pericentral canal neurons, and lateral and dorsal longitudinal tracts; the syrinx phenotype gradually evolves from a separated to a dilated type, suggesting a poor prognosis (Figure 2B). Multiple small beads gradually evolve into a single dilatation in the late stage (Figure S1A). In the later stage, the syrinx separation also tends to disappear gradually with the CC expansion, which is unfavorable to syrinx remission, and self-repair potential is not effective in compensating for progressive injury without external intervention.

In our result, the complete decompression was beneficial to the overall recovery of cilia and the syrinx solution (although the cilia were still unevenly distributed, the polarity of EPC cells and the corresponding cilia in some areas tended to increase again). Since the endogenous repair for the central SCI has some plasticity to compensate in the early state (moniliform-like), the early containment of the CC expansion is essential to prevent further deterioration of the injury, and the prevention of cilia loss could be essential for avoiding the malignant CC dilation. The moniliform-like syringomyelia with separations is a distinct phenotypic feature in the early stage, which is nearly consistent with the morphologic presentation of syringomyelia in the clinic, an early reversible state with a relatively short natural history but a better prognosis after decompression.

We hypothesize that the inability of adequate motor cilia regeneration in the presence of CSF obstruction is a key factor for non-effective relief of the syringomyelia or even exacerbated secondary SCI, so the restoration of CSF circulation has always been the central concept for preventing malignant regression of syringomyelia and promoting related SCI recovery.⁴⁹ Although the specific mechanism of the ependymal cilia in the syrinx formation is yet unknown, there did be a link between the loss of cilia and the development of syringomyelia. The closely related motile cilia might play a connecting role between CSF circulation and the CC niche. Although the separation in the moniliform stage seems to provide a certain basic “soil” for cilia recovery, clinically, even with early decompression, there are still some patients whose syrinx cannot be effectively relieved, with the possibility of continued expansion,²⁶ which in turn leads to corresponding symptoms of secondary SCI. That means it would miss the optimal period of self-repair compensatory for central spinal cord injury. The results of our animal experiment also showed that the rate of effective decompression in perfection ($\geq 25\%$) was barely about 60%. In addition to effective decompression, appropriate interventions to promote the cytoskeleton and motor cilia recovery are expected to get faster and better recovery in patients with syringomyelia.

Moreover, for that demyelination did occupy a dominant process during the pathological changes, making full use of the repair potential of oligodendrocyte lineage would be another focus of syringomyelia-related spinal cord injury research in the future.⁵⁰ Most of the endogenous potential for remyelination was derived from OPCs, with an increase from OPCs to oligodendrocytes during the syrinx development, demonstrating that the organism itself has the potential to repair the injury as part of the protective immune response. EPCs exhibit the potential to differentiate into the oligodendrocyte lineage, especially after spinal cord injury, as reported in the previous literature,^{50,51} which has a more far-reaching meaning for the repair of syringomyelia-related spinal cord injury. In particular, even with syrinx resolution after effective decompression, part of patients with expanded syrinx will suffer residual damage and

contradictory symptom-imaging dissociation. A well-studied population of EPCs in the spinal cord contains the neural stem cell (NSC) potential.⁵² EPCs, which are typically dormant, would become active in response to damage and almost exclusively produce astrocytes that form scars.^{12,52} Increased endogenous NSC activity could make it easier to repair the pathological damage.⁵³ Future therapies for syringomyelia should also include modifying the EPCs' endogenous potential in the CC, transforming the restrictive niche into a favorable one in the ependymal region by using exogenous stem cells or grafts, and modulatory chemicals or medications.

In summary, the ciliated EPC subtypes might act as one of the essential drivers during the syringomyelia development in relationship with the immunomodulation of actin and microtubule cytoskeleton dynamics. After early effective decompression, endogenous repair potential as a response to the neuroinflammation could compensate for spinal cord injury around the CC region. Effective interventions of remodeling the EPC cytoskeleton targeting ependymal cilia recovery would facilitate better regression of syringomyelia.

Limitations of the study

Although parallel bulk-seq was used for validation, with ultrastructure, IF, and single-cell RNA-seq for cell-level evidence, the main body of this paper was still phenotypic studies. But it is a critical first step in our overall research plan. Based on the pseudotime analysis, it has to be validated by the lineage tracing method in the future whether there was an EPC subgroup for enlarged oligodendrocyte transition latently with injury responsive. We observed that the abnormality of ependymal cell polarity with motile cilia damage might reflect the unrestricted expansion of the CC accompanied by the continued progression of parenchymal edema. Overall, cilia loss appears to be positively correlated with the development of syringomyelia over time series. However, the surviving cilia in separation seem to be crucial for the syringomyelia resolution after decompression. A novel perspective on the pathogenesis of canalicular syringomyelia was proposed: the obstruction of the subarachnoid space might not be the unique cause of the disease. The abnormal cytoskeleton of the CC and cilia loss could also be the contributing factors for syringomyelia development. However, the specific role of ependymal cilia in syringomyelia formation and the mechanism of cilia damage and the ultra-early observation study should be further investigated, and the core genes related to cilia regeneration and biomarkers associated with anti-inflammation could be verified in the future.

STAR★METHODS

Detailed methods are provided in the online version of this paper and include the following:

- KEY RESOURCES TABLE
- RESOURCE AVAILABILITY
 - Lead contact
 - Materials availability
 - Data and code availability
- EXPERIMENTAL MODEL AND SUBJECT DETAILS
 - Animals
- METHOD DETAILS
 - Animal experiments
 - Behavioral testing
 - *In vivo* MRI
 - Ultrastructure under the transmission and scanning electron microscopy
 - Tissue processing for histological structure observation
 - Immunofluorescence
 - Bulk RNA-Seq
 - Single-cell RNA-Seq
- QUANTIFICATION AND STATISTICAL ANALYSIS

SUPPLEMENTAL INFORMATION

Supplemental information can be found online at <https://doi.org/10.1016/j.isci.2023.106850>.

ACKNOWLEDGMENTS

We acknowledge the help of Mr. Zhanjing Wang in the magnetic resonance imaging of the rats and image processing. We thank Prof. Zixin Zhu of Xuanwu Hospital Animal Experiment Center for providing help with animal care. We express our gratitude to Dr. Xiaoyu Xue, Dr. Yongheng Fan, Dr. Rui Quan, Dr. Jiachen Wang, and Dr. Haoteng Yan for their guidance on the experimental techniques. We are also grateful to Dr. Yan Yang from the electron microscope unit, Biomedical Testing Center, Tsinghua University for providing excellent technical support.

This work was supported by grants from the Beijing Municipal Natural Science Foundation (No. 583003) funded by Beijing Municipal Science & Technology Commission (Grant number: L212007).

All applicable international, national, and/or institutional guidelines for the care and use of animals were followed. All procedures performed in studies involving animals were by the ethical standards of the institution or practice at which the studies were conducted (Experimental Animal Welfare Ethics Committee, Xuanwu Hospital, Capital Medical University, no. XWH2019002).

AUTHOR CONTRIBUTIONS

C.L.L. and F.Z.J. designed the research; C.L.L., X.Y.W., and J.W.D. performed the experiments; C.L.L. and X.M.W. analyzed the data; C.L.L., X.Y.W., and L.B.M. conducted the statistical analysis; C.L.L. and X.M.W. prepared the paper. All authors have read and approved the article.

DECLARATION OF INTERESTS

We declare there are no competing financial interests in this work.

Received: January 17, 2023

Revised: March 5, 2023

Accepted: May 4, 2023

Published: May 11, 2023

REFERENCES

- Heiss, J.D., Snyder, K., Peterson, M.M., Patronas, N.J., Butman, J.A., Smith, R.K., Devroom, H.L., Sansur, C.A., Eskioğlu, E., Kammerer, W.A., and Oldfield, E.H. (2012). Pathophysiology of primary spinal syringomyelia. *J. Neurosurg. Spine* 17, 367–380. <https://doi.org/10.3171/2012.8.Spine111059>.
- Oldfield, E.H. (2017). Pathogenesis of chiari I - pathophysiology of syringomyelia: implications for therapy: a summary of 3 decades of clinical research. *Neurosurgery* 64, 66–77. <https://doi.org/10.1093/neuros/nyx377>.
- Fehlings, M.G., and Austin, J.W. (2011). Posttraumatic syringomyelia. *J. Neurosurg. Spine* 14, 570–572. , discussion 572. <https://doi.org/10.3171/2010.4.Spine1047>.
- Leclerc, A., Matveeff, L., and Emery, E. (2021). Syringomyelia and hydromyelia: current understanding and neurosurgical management. *Rev. Neurol.* 177, 498–507. <https://doi.org/10.1016/j.neuro.2020.07.004>.
- Klekamp, J. (2012). Treatment of posttraumatic syringomyelia. *J. Neurosurg. Spine* 17, 199–211. <https://doi.org/10.3171/2012.5.Spine11904>.
- Greitz, D. (2006). Unraveling the riddle of syringomyelia. *Neurosurg. Rev.* 29, 251–263. , discussion 264. <https://doi.org/10.1007/s10143-006-0029-5>.
- Holly, L.T., and Batzdorf, U. (2019). Chiari malformation and syringomyelia. *J. Neurosurg. Spine* 31, 619–628. <https://doi.org/10.3171/2019.7.Spine181139>.
- Grassner, L., Riemenschneider, M.J., Altendorfer, B., Grillhösl, A., Arevalo-Martin, A., Garcia-Ovejero, D., Mach, O., Maier, D., Bierschneider, M., Strowitzki, M., et al. (2022). Subarachnoid fibrosis in human post-traumatic syringomyelia: a prospective observational clinical study. *J. Neuropathol. Exp. Neurol.* 81, 149–153. <https://doi.org/10.1093/jnen/nlab121>.
- Reiter, J.F., and Leroux, M.R. (2017). Genes and molecular pathways underpinning ciliopathies. *Nat. Rev. Mol. Cell Biol.* 18, 533–547. <https://doi.org/10.1038/nrm.2017.60>.
- Morimoto, Y., Yoshida, S., Kinoshita, A., Satoh, C., Mishima, H., Yamaguchi, N., Matsuda, K., Sakaguchi, M., Tanaka, T., Komohara, Y., et al. (2019). CFAP43Nonsense mutation in causes normal-pressure hydrocephalus with ciliary abnormalities. *Neurology* 92, e2364–e2374. <https://doi.org/10.1212/wnl.0000000000007505>.
- Meletis, K., Barnabé-Heider, F., Carlén, M., Evergren, E., Tomilin, N., Shupliakov, O., and Frisé, J. (2008). Spinal cord injury reveals multilineage differentiation of ependymal cells. *PLoS Biol.* 6, e182. <https://doi.org/10.1371/journal.pbio.0060182>.
- Sabelström, H., Stenudd, M., and Frisé, J. (2014). Neural stem cells in the adult spinal cord. *Exp. Neurol.* 260, 44–49. <https://doi.org/10.1016/j.expneurol.2013.01.026>.
- Xu, N., Xu, T., Mirasol, R., Holmberg, L., Vincent, P.H., Li, X., Falk, A., Benedikz, E., Rotstein, E., Seiger, A., et al. (2021). Transplantation of human neural precursor cells reverses syrinx growth in a rat model of post-traumatic syringomyelia. *Neurotherapeutics* 18, 1257–1272. <https://doi.org/10.1007/s13311-020-00987-3>.
- Xu, T., Li, X., Guo, Y., Uhlin, E., Holmberg, L., Mitra, S., Winn, D., Falk, A., and Sundström, E. (2022). Multiple therapeutic effects of human neural stem cells derived from induced pluripotent stem cells in a rat model of post-traumatic syringomyelia. *EBioMedicine* 77, 103882. <https://doi.org/10.1016/j.ebiom.2022.103882>.
- Ma, L., Yao, Q., Zhang, C., Li, M., Cheng, L., and Jian, F. (2020). Chronic extradural compression of spinal cord leads to syringomyelia in rat model. *Fluids Barriers*

- CNS 17, 50. <https://doi.org/10.1186/s12987-020-00213-4>.
16. Ono, A., Suetsuna, F., Ueyama, K., Yokoyama, T., Aburakawa, S., Numasawa, T., Wada, K., and Toh, S. (2007). Surgical outcomes in adult patients with syringomyelia associated with Chiari malformation type I: the relationship between scoliosis and neurological findings. *J. Neurosurg. Spine* 6, 216–221. <https://doi.org/10.3171/spi.2007.6.3.216>.
 17. Lu, C., Ma, L., Yuan, C., Cheng, L., Wang, X., Duan, W., Wang, K., Chen, Z., Wu, H., Zeng, G., and Jian, F. (2022). Phenotypes and prognostic factors of syringomyelia in single-center patients with chiari I malformation: moniliform type as a special configuration. *Neurospine* 19, 816–827. <https://doi.org/10.14245/ns.2244332.166>.
 18. Stenudd, M., Sabelström, H., and Frisén, J. (2015). Role of endogenous neural stem cells in spinal cord injury and repair. *JAMA Neurol.* 72, 235–237. <https://doi.org/10.1001/jamaneurol.2014.2927>.
 19. Hachem, L.D., Mothe, A.J., and Tator, C.H. (2020). Unlocking the paradoxical endogenous stem cell response after spinal cord injury. *Stem cells* (Dayton, Ohio) 38, 187–194. <https://doi.org/10.1002/stem.3107>.
 20. Li, C., Wu, Z., Zhou, L., Shao, J., Hu, X., Xu, W., Ren, Y., Zhu, X., Ge, W., Zhang, K., et al. (2022). Temporal and spatial cellular and molecular pathological alterations with single-cell resolution in the adult spinal cord after injury. *Signal Transduct. Targeted Ther.* 7, 65. <https://doi.org/10.1038/s41392-022-00885-4>.
 21. Milich, L.M., Choi, J.S., Ryan, C., Cerqueira, S.R., Benavides, S., Yahn, S.L., Tsoufas, P., and Lee, J.K. (2021). Single-cell analysis of the cellular heterogeneity and interactions in the injured mouse spinal cord. *J. Exp. Med.* 218, e20210040. <https://doi.org/10.1084/jem.20210040>.
 22. Barnabé-Heider, F., Göritz, C., Sabelström, H., Takebayashi, H., Pfrieger, F.W., Meletis, K., and Frisén, J. (2010). Origin of new glial cells in intact and injured adult spinal cord. *Cell Stem Cell* 7, 470–482. <https://doi.org/10.1016/j.stem.2010.07.014>.
 23. Li, X., Floriddia, E.M., Toskas, K., Fernandes, K.J.L., Guéroul, N., and Barnabé-Heider, F. (2016). Regenerative potential of ependymal cells for spinal cord injuries over time. *EBioMedicine* 13, 55–65. <https://doi.org/10.1016/j.ebiom.2016.10.035>.
 24. Brennan, F.H., Li, Y., Wang, C., Ma, A., Guo, Q., Li, Y., Pukos, N., Campbell, W.A., Witcher, K.G., Guan, Z., et al. (2022). Microglia coordinate cellular interactions during spinal cord repair in mice. *Nat. Commun.* 13, 4096. <https://doi.org/10.1038/s41467-022-31797-0>.
 25. Li, Y., He, X., Kawaguchi, R., Zhang, Y., Wang, Q., Monavarfeshani, A., Yang, Z., Chen, B., Shi, Z., Meng, H., et al. (2020). Microglia-organized scar-free spinal cord repair in neonatal mice. *Nature* 587, 613–618. <https://doi.org/10.1038/s41586-020-2795-6>.
 26. Hatem, S.M., Attal, N., Ducreux, D., Gautron, M., Parker, F., Plaghki, L., and Bouhassira, D. (2010). Clinical, functional and structural determinants of central pain in syringomyelia. *Brain* 133, 3409–3422. <https://doi.org/10.1093/brain/awq244>.
 27. Zhang, Y.P., Zhang, Y., Shields, L.B.E., Zheng, Y., Xu, X.M., Whittemore, S.R., and Shields, C.B. (2012). Cervical central canal occlusion induces noncommunicating syringomyelia. *Neurosurgery* 71, 126–137. <https://doi.org/10.1227/NEU.0b013e31824d18ae>.
 28. Hemley, S.J., Bilston, L.E., Cheng, S., and Stoodley, M.A. (2012). Aquaporin-4 expression and blood-spinal cord barrier permeability in canalicular syringomyelia. *J. Neurosurg. Spine* 17, 602–612. <https://doi.org/10.3171/2012.9.Spine1265>.
 29. Shields, C.B., Zhang, Y.P., and Shields, L.B.E. (2012). Post-traumatic syringomyelia: CSF hydrodynamic changes following spinal cord injury are the driving force in the development of PTSM. *Handb. Clin. Neurol.* 109, 355–367. <https://doi.org/10.1016/b978-0-444-52137-8.00022-x>.
 30. Ridlen, R., McGrath, K., and Gorrie, C.A. (2022). Animal models of compression spinal cord injury. *J. Neurosci. Res.* 100, 2201–2212. <https://doi.org/10.1002/jnr.25120>.
 31. Lee, J.Y., Kim, S.W., Kim, S.P., Kim, H., Cheon, J.E., Kim, S.K., Paek, S.H., Pang, D., and Wang, K.C. (2017). A rat model of chronic syringomyelia induced by epidural compression of the lumbar spinal cord. *J. Neurosurg. Spine* 27, 458–467. <https://doi.org/10.3171/2016.9.Spine16188>.
 32. Voelz, K., Kondziella, D., von Rautenfeld, D.B., Brinker, T., and Lüdemann, W. (2007). A ferritin tracer study of compensatory spinal CSF outflow pathways in kaolin-induced hydrocephalus. *Acta Neuropathol.* 113, 569–575. <https://doi.org/10.1007/s00401-007-0203-z>.
 33. Najafi, E., Bilston, L.E., Song, X., Bongers, A., Stoodley, M.A., Cheng, S., and Hemley, S.J. (2016). Longitudinal measurements of syrinx size in a rat model of posttraumatic syringomyelia. *J. Neurosurg. Spine* 24, 941–948. <https://doi.org/10.3171/2015.10.Spine15538>.
 34. Takagishi, M., Sawada, M., Ohata, S., Asai, N., Enomoto, A., Takahashi, K., Weng, L., Ushida, K., Ara, H., Matsui, S., et al. (2017). Daple coordinates planar polarized microtubule dynamics in ependymal cells and contributes to hydrocephalus. *Cell Rep.* 20, 960–972. <https://doi.org/10.1016/j.celrep.2017.06.089>.
 35. Takagishi, M., Esaki, N., Takahashi, K., and Takahashi, M. (2020). Cytoplasmic dynein functions in planar polarization of basal bodies within ciliated cells. *iScience* 23, 101213. <https://doi.org/10.1016/j.isci.2020.101213>.
 36. Patel, M., and Tsiokas, L. (2021). Insights into the regulation of ciliary disassembly. *Cells* 10. <https://doi.org/10.3390/cells10112977>.
 37. Saito, M., Otsu, W., Hsu, K.S., Chuang, J.Z., Yanagisawa, T., Shieh, V., Kaitsuka, T., Wei, F.Y., Tomizawa, K., and Sung, C.H. (2017). Tctex-1 controls ciliary resorption by regulating branched actin polymerization and endocytosis. *EMBO Rep.* 18, 1460–1472. <https://doi.org/10.15252/embr.201744204>.
 38. Hol, E.M., and Pekny, M. (2015). Glial fibrillary acidic protein (GFAP) and the astrocyte intermediate filament system in diseases of the central nervous system. *Curr. Opin. Cell Biol.* 32, 121–130. <https://doi.org/10.1016/j.ceb.2015.02.004>.
 39. Kriegstein, A., and Alvarez-Buylla, A. (2009). The glial nature of embryonic and adult neural stem cells. *Annu. Rev. Neurosci.* 32, 149–184. <https://doi.org/10.1146/annurev.neuro.051508.135600>.
 40. Capilla-Gonzalez, V., Cebrian-Silla, A., Guerrero-Cazares, H., Garcia-Verdugo, J.M., and Quiñones-Hinojosa, A. (2014). Age-related changes in astrocytic and ependymal cells of the subventricular zone. *Glia* 62, 790–803. <https://doi.org/10.1002/glia.22642>.
 41. Silvin, A., Uderhardt, S., Piot, C., Da Mesquita, S., Yang, K., Geirsdottir, L., Mulder, K., Eyal, D., Liu, Z., Bridlance, C., et al. (2022). Dual ontogeny of disease-associated microglia and disease inflammatory macrophages in aging and neurodegeneration. *Immunity* 55, 1448–1465.e6. <https://doi.org/10.1016/j.immuni.2022.07.004>.
 42. Trujillo-Cenóz, O., Rehmann, M.I., Maciel, C., Falco, M.V., Fabbiani, G., and Russo, R.E. (2021). The ependymal cell cytoskeleton in the normal and injured spinal cord of mice. *J. Neurosci. Res.* 99, 2592–2609. <https://doi.org/10.1002/jnr.24918>.
 43. Davidson, A.J., and Wood, W. (2016). Unravelling the actin cytoskeleton: a new competitive edge? *Trends Cell Biol.* 26, 569–576. <https://doi.org/10.1016/j.tcb.2016.04.001>.
 44. Thouvenin, O., Keiser, L., Cantaut-Belarif, Y., Carbo-Tano, M., Verweij, F., Jurisch-Yaksi, N., Bardet, P.L., van Niel, G., Gallaire, F., and Wyart, C. (2020). Origin and role of the cerebrospinal fluid bidirectional flow in the central canal. *Elife* 9, e47699. <https://doi.org/10.7554/eLife.47699>.
 45. Mahuzier, A., Shihavuddin, A., Fournier, C., Lansade, P., Faucourt, M., Menezes, N., Meunier, A., Garfa-Traoré, M., Carlier, M.F., Voituriez, R., et al. (2018). Ependymal cilia beating induces an actin network to protect centrioles against shear stress. *Nat. Commun.* 9, 2279. <https://doi.org/10.1038/s41467-018-04676-w>.
 46. Zhang, J., Chandrasekaran, G., Li, W., Kim, D.Y., Jeong, I.Y., Lee, S.H., Liang, T., Bae, J.Y., Choi, I., Kang, H., et al. (2020). Wnt-PLC-IP-Connexin-Ca axis maintains ependymal motile cilia in zebrafish spinal cord. *Nat. Commun.* 11, 1860. <https://doi.org/10.1038/s41467-020-15248-2>.
 47. Hu, H.B., Song, Z.Q., Song, G.P., Li, S., Tu, H.Q., Wu, M., Zhang, Y.C., Yuan, J.F., Li, T.T., Li, P.Y., et al. (2021). LPA signaling acts as a cell-extrinsic mechanism to initiate cilia disassembly and promote neurogenesis. *Nat.*

- Commun. 12, 662. <https://doi.org/10.1038/s41467-021-20986-y>.
48. Li, Y.C., Bai, W.Z., Sakai, K., and Hashikawa, T. (2009). Fluorescence and electron microscopic localization of F-actin in the ependymocytes. *J. Histochem. Cytochem.* 57, 741–751. <https://doi.org/10.1369/jhc.2009.953646>.
 49. Xiong, G., Elkind, J.A., Kundu, S., Smith, C.J., Antunes, M.B., Tamashiro, E., Kofonow, J.M., Mitala, C.M., Cole, J., Stein, S.C., et al. (2014). Traumatic brain injury-induced ependymal ciliary loss decreases cerebral spinal fluid flow. *J. Neurotrauma* 31, 1396–1404. <https://doi.org/10.1089/neu.2013.3110>.
 50. Llorens-Bobadilla, E., Chell, J., Le Merre, P., Wu, Y., Zamboni, M., Bergensträhle, J., Stenudd, M., Sopova, E., Lundeberg, J., Shupliakov, O., et al. (2020). A latent lineage potential in resident neural stem cells enables spinal cord repair. *Science* 370. <https://doi.org/10.1126/science.abb8795>.
 51. Frederico, B., Martins, I., Chapela, D., Gasparini, F., Chakravarty, P., Ackels, T., Piot, C., Almeida, B., Carvalho, J., Ciccarelli, A., et al. (2022). DNGR-1-tracing marks an ependymal cell subset with damage-responsive neural stem cell potential. *Dev. Cell* 57, 1957–1975.e9. <https://doi.org/10.1016/j.devcel.2022.07.012>.
 52. Becker, C.G., Becker, T., and Hugnot, J.P. (2018). The spinal ependymal zone as a source of endogenous repair cells across vertebrates. *Prog. Neurobiol.* 170, 67–80. <https://doi.org/10.1016/j.pneurobio.2018.04.002>.
 53. Liu, S., and Chen, Z. (2019). Employing endogenous NSCs to promote recovery of spinal cord injury. *Stem Cell. Int.* 2019, 1958631. <https://doi.org/10.1155/2019/1958631>.
 54. Nardone, R., Höller, Y., Thomschewski, A., Bathke, A.C., Ellis, A.R., Golaszewski, S.M., Brigo, F., and Trinka, E. (2015). Assessment of corticospinal excitability after traumatic spinal cord injury using MEP recruitment curves: a preliminary TMS study. *Spinal Cord* 53, 534–538. <https://doi.org/10.1038/sc.2015.12>.
 55. Cheng, X.H., Zhang, L., and Fu, J. (2019). Somatosensory evoked potential changes and decompression timing for spinal cord function recovery and evoked potentials in rats with spinal cord injury. *Brain Res. Bull.* 146, 7–11. <https://doi.org/10.1016/j.brainresbull.2018.12.003>.

STAR★METHODS

KEY RESOURCES TABLE

REAGENT or RESOURCE	SOURCE	IDENTIFIER
Antibodies		
rabbit anti-NeuN	Abcam	Cat#177487
mouse anti-Beta III Tubulin	MAB	Cat#5564
rat anti-Nestin	BD biosciences	Cat#556309
goat anti-Foxj1	Affinity Biosciences LTD	Cat#3619
mouse anti-Sox2	Abcam	Cat#79351
mouse anti-GFAP	Abcam	Cat#360
mouse anti-Alpha Tubulin	Servicebio Biological	Cat#GB12200
goat anti-Sox9	Affinity Biosciences LTD	Cat#3075
mouse anti-Gamma tubulin	Sigma	Cat#T6557
rabbit anti-Arl13b	Proteintech Group	Cat#17711-1-AP
rabbit anti-Sox10	Abcam	Cat#155279
rabbit anti-Olig2	Abcam	Cat#109186
rabbit anti-CD68	Abcam	Cat#125212
goat anti-IBA1	Abcam	Cat#5076
rat anti-MBP	Abcam	Cat#7349
goat anti-PDGFR α	Affinity Biosciences LTD	Cat#307-NA
rat anti-BrdU	Abcam	Cat#6326
Chemicals, peptides, and recombinant proteins		
PDS Kit, Papain Vial	Solarbio	Cat#EX5000
Paraformaldehyde	Sigma-Aldrich	Cat#158127
OCT Compound	SAKURA	Cat#4583
Sucrose	Sigma-Aldrich	Cat#V900116
5-Bromo-2'-deoxyuridine (BrdU)	Sigma-Aldrich	Cat#59-14-3
F-actin	Servicebio Biological	Cat#CR2203082
Critical commercial assays		
RNA Nano6000 assay kit	Agilent Technologies	Bioanalyzer 2100 system
MGI Easy RNA library preparation kit	MGI	N/A
DNBelab C series single-cell RNA library preparation kit	MGI	N/A
DNBSEQ	MGI	T7
DNBelab	MGI	C4
Deposited data		
Bulk RNA-seq	This study, GEO	GEO: GSE217697
Single-cell RNA-seq	This study, GEO	GEO: GSE218106
Experimental models: Organisms/strains		
Sprague-Dawley rats for Sham group	Charles River Laboratories	CrI: CD(SD)101
Sprague-Dawley rats for Syringomyelia group	Charles River Laboratories	CrI: CD(SD)101
Sprague-Dawley rats for Decompression group	Charles River Laboratories	CrI: CD(SD)101

(Continued on next page)

Continued

REAGENT or RESOURCE	SOURCE	IDENTIFIER
<i>Software and algorithms</i>		
ImageJ v 1.8.0	NIH	https://imagej.nih.gov/ij/
GraphPad Prism v 9.0.0	GraphPad Software	https://www.graphpad.com/features
Leica Application Suite X	Leica Corp	Leica Microsystems
Metascape v 3.5.2	NIH	http://metascape.org/
Cytoscape v 3.9.1	Cytoscape.js	https://cytoscape.org/
Seurat R package v 4.0.1	cran.r-project.org	N/A
Monocle R package v 2.18.0	cran.r-project.org	N/A
DNBC4tools v 2.3.0	DNBelab C4	N/A

RESOURCE AVAILABILITY

Lead contact

Further information and requests for resources and reagents should be directed to and will be fulfilled by the Lead Contact, Fengzeng Jian (jianfengzeng@xwh.ccmu.edu.cn).

Materials availability

This study did not generate new unique reagents.

Data and code availability

Single-cell and bulk RNA-seq data have been deposited at GEO and are publicly available as of the date of publication. Accession numbers are listed in the [key resources table](#).

All original code and any additional information required to reanalyze the data reported in this paper are available from the [lead contact](#) upon reasonable request.

EXPERIMENTAL MODEL AND SUBJECT DETAILS

Animals

Sprague-Dawley rats in this study were ordered from Beijing Vital River Laboratory Animal Technology Corp (a joint venture of Charles River Laboratories, USA). At the age of 8-week-old, the female rats with body weight ranging from 180 to 230 g were randomly divided into three groups.

The animal experiments conformed to the standards of the Animal Welfare Committees of Capital Medical University in Beijing, China. The Rats were housed in standard sterile conditions in a 12-hour light/dark cycle (temperature: 20 - 26°C, humidity: 40 - 70%), with free access to food and water at the Animal Experiment Center of China-International Neuroscience Institute (China-INI).

METHOD DETAILS

Animal experiments

A total of 130 female Sprague-Dawley rats were divided into three groups: (1) the Control group (Sham group) included 18 rats sham-operated; (2) the Experimental group (Operation group) all received extradural compression including 112 rats with syring confirmed by MRI at Sham, 2 weeks, 4 weeks, 6 weeks after syringomyelia induction, and they were randomly divided into two subgroups: 84 rats for natural observation of the syringomyelia (Syringomyelia group) and 28 rats for decompression operation at post-op 4w (Decompression group, or 6w-).

All animal operations were performed under general anesthesia with a dose of 0.5-2% enflurane delivered in an oxygen-enriched inhalant. They were operated under a surgical microscope (OPMI Pico, Carl Zeiss, Oberkochen, Germany) under the 16× or 25× field of view. Wound healing, egestion, excretion, and body weight were monitored daily for all animals with antibiotics (cefuroxime) injected intraperitoneally for 3 days after the operation.

Behavioral testing

BBB locomotor scoring

For all rats in the operation group and the sham group, Basso, Beattie, and Bresnahan (BBB) scoring ranged from 0 (completely paralyzed) to 21 (healthy) were evaluated weekly before and after the operation by two observers without awareness of the operation group conditions in a double-blinded manner. The hind limb locomotor function of the rats was evaluated in an open walking field.

Neurological electrophysiology analysis

Electrophysiological testing was performed for each group per week after the operation, which was measured with motor-evoked potential (MEP)⁵⁴ and somatosensory-evoked potential (SEP)⁵⁵ by a keypoint channel-evoked potential/electromyography system (9033A07, Dantech Corp, Copenhagen, Denmark). Two features of evoked potential were recorded at the gastrocnemius muscle of the hindlimb for MEP and the parietal central zero (Cz) for SEP: peak-to-peak amplitudes were calculated as amplitude values and the onset time of the first response to the stimulus was measured as latency. Since SEP included mainly long conduction tracts representing deep sensory as well as part of the transmission tracts of superficial sensory, which required further identification of the superficial sensory abnormalities in correspondence with the typical segmental dissociative sensory disturbance in syringomyelia.

Von Frey hair test

Segmental sensory abnormality is the typical clinical symptom of central SCI secondary to canalicular syringomyelia. We roughly estimated the pain thresholds for mechanical pain in the corresponding segment of the syrinx. This was done weekly after operation by Von Frey hairs ranging from 0.008g-300g. Starting with the thinnest filament, rats were tested by increasing pressure on the corresponding sensory sites until an avoidance response occurred. Once there is a response, the next lower-force filament is tested. The mechanical withdrawal threshold of each rat was defined using the “up-down” method which at least four readings are obtained after the first change of direction.

Hot plate test

In the hot plate test, the rat is placed on a metal surface maintained at a constant temperature ($52 \pm 0.5^\circ\text{C}$, Ambient temperature between 20°C and 25°C), and the time taken to elicit a nocifensive behavior (e.g., hind paw withdrawal or licking) is recorded by Hot/Cold-Plate Analgesia Meter (BIO-CHP, France, bioseb). If the subject did not show such a response within 50 seconds, that would be removed from the device and the test terminated. There may be no benefit in repeating the trial.

In vivo MRI

All rats (operation group: $n = 112$ and sham group: $n = 18$) underwent serial MRI scans for 2 weeks after the operation. *In vivo* MRI was performed using a 7.0 Tesla MRI scanner (PharmaScan 7T, Bruker Corp., Karlsruhe, Germany) with 400 mT/m gradients in the Animal Imaging Experimental Center at Capital Medical University. Centered on the operation site, the sagittal and axial T2-weighted images were acquired by a fat-saturated RARE sequence. A rat volume coil with a diameter of 89 mm was used for transmission and to obtain data.

All measurements in the T2-weighted images were made using RadiAnt DICOM Viewer software (Version 4.6.9, Medixant, Poznan, Poland). The maximal anteroposterior diameter (D1) and transverse syrinx area (S1) of the syrinx were measured. The spinal cord anteroposterior diameter (D2) and transverse syrinx area (S2) at the same level were also measured. The ratio of n/m and $D1/D2$ were calculated to evaluate the change of the syrinx.

Ultrastructure under the transmission and scanning electron microscopy

The rats in both groups after excessive inhalation of isoflurane were intracardially perfused with 4% polyformaldehyde in phosphate buffer saline (PBS, pH 7.4, Sigma). Spinal cord tissue in a mixture of paraformaldehyde (2%) and glutaraldehyde (2.5%) was stored at 4°C and then washed 4 times with PB buffer (0.1 M). Finally, the spinal cord was dissected and processed for electron microscopy.

Tissue blocks for SEM were dissected longitudinally to expose the canal surfaces, dehydrated in gradient ethanol (50%, 70%, 80%, 90%, 100%, 100%, 100%) sequentially for 15 min each, and taken to a critical point.

The CC surface was studied under the environmental scanning electron microscope (ESEM) Quanta 200 (FEI, Hillsboro, America).

The spinal cord segments (1 mm thick) for TEM underwent post-fixation with Osmium tetroxide (1%) and Tetrapotassium hexacyanoferrate trihydrate (1.5%) for 1 h, followed by ethanol dehydration in graded solutions for 10 min each. Ultra-thin sections (70 nm) were mounted and dried on coated copper grids. Imaging was carried out using Hitachi 7650B (transmission electron microscopy). The ultrastructure of the ependymal region was examined in at least three sections from the separate spinal cord levels of the syrinx segments in four repetitions of each group.

Tissue processing for histological structure observation

After excessive inhaling of isoflurane, the rats were transcardially perfused with 4% polyformaldehyde (PFA, Sigma) in PBS. The spinal cord was removed and placed overnight in 4% PFA at 4 °C, then transferred to 30% sucrose (Sigma) twice and placed overnight at 4 °C. A spinal cord segment (25 mm length centered on the syrinx core) was encapsulated using embedding media, OCT (Sakura Corp., Tokyo, Japan) on dry ice. Tissue sections were cut at a thickness of 15 μm using a Microtome-Cryostat (CM3050 S, Leica Biosystems, Nussloch, Germany), and mounted on charged glass slides. The sections were stained by hematoxylin-eosin (H-E, Sigma) to observe the histological structure of the tissue after SCI.

Immunofluorescence

Sections were washed with 1 × (0.01 M) PBS and incubated with the primary antibodies at 4 °C overnight after 1 h blocking by 5% normal goat serum (NGS, Sigma) and 0.3% Triton X-100 (Sigma). The sections were then incubated at room temperature for 1 h with fluorescent-labeled secondary antibodies (Invitrogen) and washed with 0.01 M PBS 3 times before being observed under a confocal laser scanning microscope (STELLARIS 5, Leica Corp., Wetzlar, Germany). Fluorescence immunohistochemistry was performed using the following primary antibodies: rabbit anti-NeuN (Abcam177487, 1:500), mouse anti-Beta III Tubulin (Tuj1, MAB5564, 1:500), rat anti-Nestin (BD Biosciences, 556309, 1:500), goat anti-Foxj1 (AF3619, 1:500), mouse anti-Sox2 (Abcam79351, 1:500), mouse anti-GFAP (Abcam360, 1:500), F-actin (stain 488, Servicebio, CR2203082, 1:300), mouse anti-Alpha Tubulin (Servicebio, GB12200, 1:1000), goat anti-Sox9 (AF3075, 1:500), mouse anti-Gamma tubulin (Sigma, T6557, 1:500), rabbit anti-Arl13b (Proteintech, 17711-1-AP, 1:500), rabbit anti-Sox10 (Abcam155279, 1:500), rabbit anti-Olig2 (Abcam109186), rabbit anti-CD68 (Abcam125212, 1:500), goat anti-IBA1 (Abcam5076, 1:500), rat anti-MBP (Abcam7349, 1:500), goat anti-PDGFRα (AF307-NA, 1:50), and rat anti-BrdU (ab6326). Cell nuclei were stained with DAPI (Invitrogen).

BrdU and BrdU-labeled section immunostaining

5-Bromo-2'-deoxyuridine (BrdU, Sigma-Aldrich) was dissolved in PBS (10 mg/ml). Animals received daily intraperitoneal injections of BrdU (50 mg/kg) for 14 days following surgery in both sham and operation groups. DNA hydrolysis step was required before the standard immunostaining process. Sections were incubated in 1 mol/L HCL for 30 min at 37 °C, neutralized with 0.1 mol/L sodium borate buffer for 10 min at room temperature, and then washed three times with PBS. The sections were then subjected to standard immunostaining protocols.

Image quantification

For animals ($n \geq 4$) in each group, longitudinal slices containing the central spinal canal were selected and transverse slices were selected at the largest site of syringomyelia. The target areas were photographed by the objective lens of 10×, 20×, or 40× (oil) or with optical zoom using confocal laser scanning microscopy at a resolution of 1024 × 1024 pixels. Each region was scanned along the z-step size of 1–3 μm. The final 3-D image was achieved by reconstructing these consecutive scans using the Leica Application Suite X (Leica Microsystems, Leica Corp., Wetzlar, Germany). We then used Leica Suite X to determine cell counts, mean fluorescent intensity, and regions of interest. All figures were composed with Adobe Photoshop and Adobe Illustrator.

Bulk RNA-Seq

The 15 mm long spinal cord tissues located at the syrinx segments judged by MRI, including sham and operation group, were collected corresponding to different time points after the operation (2w, 4w, 6w, and 4w

decompression-6w). The tissues were homogenized in 1 mL TRIzol (Invitrogen) for further purification and RNA-seq.

The purity of RNA was determined by NanoPhotometer (IMPLEN, CA, USA). The RNA integrity and concentration were assessed using the RNA Nano6000 Assay Kit of the Bioanalyzer 2100 system (Agilent Technologies, CA, USA). Qualified RNA was subjected to construct a double-stranded PCR library using the MGI Easy RNA library preparation kit. Sequencing was performed on DNBSEQ-T7 and 150bp double-ended sequencing reads were obtained.

The raw data processing pipeline

Raw paired-end reads were trimmed by trimmomatic v0.39. Clean reads were mapped to the *Rattus norvegicus* Ensembl.Rnor.v 6.0.89 reference genome using HISAT2 (version 2.1.0). The sam files were converted to bam files by SAMtools with the parameter “-S -b”. Then, read counts were calculated by HTSeq (version 0.6.0), and only high-quality mapped reads (mapping quality > 20) were retained. The Fragments Per Kilobase per Million (FPKM) value for each gene was calculated to estimate the expression level of genes in each sample.

Analysis of differential expression

Differentially expressed genes (DEGs) were calculated using the DESeq2 package (version 1.22.2) with the cutoff “q value (adjusted p-value, padj) < 0.05 and | log₂ (fold change) | > 1. Gene Ontology (GO) enrichment analysis was conducted with Metascape and visualized by Cytoscape (version 3.9.1).

Single-cell RNA-Seq

The sampling range of single-cell sequencing was the same as that of bulk RNA-seq. (Figure 1D) The tissues cut into approximately 0.5-mm³ pieces in the PBS were dissociated using a PDS Kit, Papain Vial (Solarbio) with a concentration of 25 U/ml in EBSS (Invitrogen). The tissue was digested at a constant temperature of 37°C for one hour and gently blown with fire-polished Pasteur pipettes every 10 minutes. The single-cell suspension was filtered through a 40 μm cell strainer and then centrifuged at 400 r/min for 5 min at 4 °C. The pellet was washed with DMEM (Invitrogen) containing 0.1% bovine serum albumin (BSA). Cell viability was assessed by trypan blue staining. The cells were diluted to a final concentration of 1 × 10⁶/ml.

The mRNA capture was operated on a DNBelab C4 device (MGI). The volume of single-cell suspension that was required to generate 10,000 single-cell GEMs (gel beads in the emulsion) per sample. Libraries were prepared using the MGI DNBelab C series single-cell RNA library preparation kit according to the manufacturer’s specifications. Final library quantification and quality control were performed using a Qubit 3.0 and LabChip GX Touch, followed by sequencing on the DNBSEQ-T7 sequencing platform.

The raw data processing pipeline

Raw sequence data were aligned to the ENSEMBL database (*Rattus norvegicus* Ensembl.Rnor.v 6.0.89 reference genome), and cell numbers along with unique molecular identifiers (UMIs) were estimated by DNBC4tools, the single-cell software suite from DNBelab C4v2.3. Downstream analyses were performed using the Seurat R package (version 4.0.1). Low-quality cells with less than 200 genes expressed and more than 10% mitochondria content were filtered.

Clustering and cell-type classification

Gene expression matrices were obtained by DNBelab C4, and highly variable genes were selected by the FindVariableFeatures function (VST method) for downstream principal component analysis. By a combination of the “JackStraw” and “ElbowPlot” results of Seurat, the top 20 principal components of PCA results were selected, and a graph-based clustering method was used to classify cells. The clustering results were visualized using UMAP plots. The function FindAllMarkers was used to find the DEGs in each cluster. Cell types were identified by marker genes from the literature.

Analysis of ependymal cells, macrophages, microglia, oligodendrocyte precursor cells, and oligodendrocytes. All samples were integrated by Seurat based on first identifying cross-dataset pairs of cells that are in a matched biological state (“anchors”). Functions “FindIntegrationAnchors” and “Integrate-Data” were used to correct batch effects from technical differences between datasets and perform a

comparative analysis across experimental conditions. Then, for different cell types (ependymal cells, macrophages, microglia, oligodendrocyte precursor cells, and oligodendrocytes), we took subsets from the integrated Seurat object and redid clustering pipeline separately.

Differential gene expression testing and GO annotation

To identify marker genes for each cluster, we performed the FindAllMarkers function using default parameters, which implements a Wilcoxon rank-sum test comparing gene expression of cells within a given cluster versus all other cells. We repeated this test for each of the three compartments to identify marker genes for each subtype. To identify DEGs for GO analysis, the Seurat FindMarkers function and our customized R scripts were used to figure out significantly ($p < 0.05$) up-regulated ($\log_{2}(\text{fold change}) = 0.25$) and down-regulated ($\log_{2}(\text{fold change}) = -0.25$) genes. For GO analysis, cluster Profiler (3.18.1) and the "org.Rn.eg.db" package were used to annotate differentially expressed genes (p -value cutoff = 0.05). For analysis of OPCs and oligodendrocytes over time, we compared cells from each sequential time point and took all DEGs with an average log foldchange > 0.25 and adjusted P values < 0.05 . We excluded EPCs (Cluster 1,2,3,4) from all EPCs in these comparisons because the lineage of EPCs (Cluster 1,2,3,4) may be different from canonical EPCs with oligo-differentiation potential. We compared GO terms between OPC-A and OPC-B using the DEGs with adjusted P values < 0.05 .

Pseudotime trajectory analysis of ependymal cells and oligodendrocytes

Pseudotime analysis was performed on a filtered subset of EPCs from the Seurat integrated data by using the Monocle (2.18.0) R package. Gene order was performed by using a cutoff of expression in at least 10 cells and a combination of intercluster differential expression and dispersion with a q -value cutoff of < 0.01 . The effects from sample differences were subtracted ($\text{residualModelFormulaStr} = \sim \text{orig.ident}$) when computing a projection of a monocle CellDataSet object into a lower dimensional space. The structure of the trajectory was plotted in 2-dimensional space using the DDRTree dimensionality reduction algorithm, and the cells were ordered in pseudotime.

QUANTIFICATION AND STATISTICAL ANALYSIS

For continuous variables, the mean values are presented with standard deviations. The differences between the two groups were analyzed using the student's T -test and One-Way ANOVA test for ≥ 3 groups. P -value < 0.05 was considered statistically significant. All quantification was performed blindly by assigning a code letter to each rat and deciphering this code only after all data analyses were complete. Statistical evaluations were conducted using GraphPad Prism (version 9.0, San Diego, USA).